Title
Nanopillar Photovoltaics: Photon Management and Junction Engineering for Next-Generation Solar Cells

Author
Mariani, Giacomo

Publication Date
2013

Peer reviewed|Thesis/dissertation

UNIVERSITY OF CALIFORNIA

Los Angeles

Nanopillar Photovoltaics: Photon Management and Junction Engineering for Next-Generation Solar Cells

A dissertation submitted in partial satisfaction of the

requirements for the degree Doctor of Philosophy

in Electrical Engineering

by

Giacomo Mariani

2013

To my exceptional parents and caring sister

ABSTRACT OF THE DISSERTATION

Nanopillar Photovoltaics: Photon Management and Junction Engineering for Next-Generation Solar Cells

by

Giacomo Mariani

Doctor of Philosophy in Electrical Engineering

University of California, Los Angeles, 2013

Professor Diana L. Huffaker, Chair

The sun delivers an amount of energy equivalent to ninety billion hydrogen bombs detonating each second. Despite the fact that only one billionth of that energy falls onto the surface of the Earth, one day of sunlight would be sufficient to power the whole human race energy needs for over half a century. Solar electricity represents an environmentally-benign source of power. However, such technology is still more than twice as expensive as natural gas-fired generators. III-V semiconductor nanopillars are defined as vertically aligned arrays of nanostructures that hold the promise to aggressively diminish the cost of the active photovoltaic cell by exploiting a fraction of material utilized in conventional planar schemes. In this dissertation, we assess the viability of two classes of high-performance nanopillar-based solar cells. We begin with the incorporation of dedicated conjugated polymers to achieve a hybrid organic/inorganic heterojunction. Such configuration introduces a high optical absorption arising from the polymeric layer in conjunction with an efficient carrier transport resulting from the

semiconductor nanopillar array. We extend the controllability of the heterojunction properties by replacing traditional spin-casting methods with an electrodeposition technique where the polymer is formed and doped in-situ directly onto the nanopillar facets. The rational tuning of the electrical conductivity and energy level of the polymer translates into an enhanced photocurrent and open-circuit voltage, achieving 4.11% solar power conversion efficiency. We then turn our attention to all-semiconductor radial p-n homojunctions embedded in the nanopillars. The first architecture focuses on ex-situ ammonium-sulfide passivation and correlates the optoelectronic properties of the solar cell once two different types of transparent conducting oxides are adopted. The barrier formed at the contact/semiconductor interface greatly depends on the Hall polarity of the transparent electrode. The second design delves into an in-situ InGaP passivation shell to alleviate the deleterious recombination effects caused by surface states. The efficiency improvement is over six-fold, up to 6.63%, compared to unpassivated devices. Lastly, a p-i-n radial junction nanopillar solar cell highlights external quantum efficiencies in great agreement with numerical simulations. In such framework, the dome morphology of the top transparent contact is found to concentrate and intensify the optical field within the nanopillar active volume, resulting into resonance peaks in the quantum yield measurements, at 7.43% efficiency. These findings confirm the potential of 3D nanopillar solar cells as a cost-effective platform with respect to canonical thin-film photovoltaics.

The dissertation of Giacomo Mariani is approved.

Yahya Rahmat-Samii

Yang Yang

Diana L. Huffaker, Committee Chair

University of California, Los Angeles

2013

Table of Contents

Symbols and acronyms

2D	Two dimensional	*J-V*	Current density - voltage
3D	Three dimensional	*EQE*	External quantum efficiency
R	Reflectance	SPCM	Scanning photocurrent microscopy
R_S	Series resistance	XPS	X-ray photoelectron spectroscopy
$\vec{E}$	Electric field	CV	Cyclic voltammetry
ε''	Imaginary part of permittivity	FDTD	Finite-difference time-domain
n	Ideality factor	SAE	Selective area epitaxy
σ	Conductivity	RF	Radio frequency
η	Power conversion efficiency	SEM	Scanning electron microscopy
Å	Armstrong	TEM	Transmission electron microscopy
v/v%	Volume-volume percentage	G_{ph}	Photogeneration
wt%	Weight percentage	PV	Photovoltaic
$n_{air,GaAs}$	Air (GaAs) refractive index	NP	Nanopillar
III-V	Group III - group V compound semiconductors	NW	Nanowire
II-VI	Group II - group VI compound semiconductors	HSC	Hybrid solar cell
V_{OC}	Open-circuit voltage	ARC	Antireflection coating
J_{SC}	Short-circuit current density	VLS	Vapor-liquid-solid
FF	Fill factor	HOMO	Highest occupied molecular orbital
PCE	Power conversion efficiency	TCO	Transparent conducting oxide
I_{SC}	Short-circuit current	ITO	Indium tin oxide

AZO	Aluminum zinc oxide	DMZn	Di-methyl-zinc
$I_{PH,SUB}$	Substrate photocurrent	C_{60}	Fullerene
$I_{PH,ARRAY}$	Array photocurrent	PSS^-	Poly-(styrenesulfonate)
I-V	Current -voltage	DS^-	Dodecyl sulfate
GaAs	Gallium arsenide	ClO_4^-	Perchlorate
InAs	Indium arsenide	BF_4^-	Tetrafluoroborate
InGaP	Indium gallium phosphide	PF_6^-	Hexafluorophosphate
Au	Gold	BCB	Benzocyclobutene
AuGe	Gold-germanium	$(NH_4)_2S$	Ammonium sulfide
Ni	Nickel	SiN_x	Silicon nitride
Ti	Titanium	SiO_2	Silicon dioxide
MOCVD	Metal organic chemical vapor deposition		
MBE	Molecular beam epitaxy		
P3HT	Poly(3-hexylthiophene-2,5-diyl)		
PEDOT	Poly(3,4-thylenedioxythiophene)		
TMGa	Tri-methyl-gallium		
TBA	Tertiary-butyl-arsine		
TBP	Tertiary-butyl-phosphine		
TMIn	Tri-methyl-indium		
TESn	Tetra-ethyl-tin		

Acknowledgements

It is fairly challenging to condense and distill in one section over four years of life-changing experience. I embarked on this journey with an open scientific curiosity, a passion for discovery that shaped me both personally and professionally as an individual. First and foremost, I am deeply thankful to my research advisor and committee chair Prof. Diana L. Huffaker. Diana instilled in me motivational and educational skills that bridge several disciplines. Her rigor for innovative research offered me to take part to several scientific conferences, file for intellectual property, and compose two book chapters, along with publishing several first-author papers in world-class peer-reviewed journals. I would like to thank my doctoral committee members Prof. Yahya Rahmat-Samii, Prof. Oscar Stafsudd, and Prof. Yang Yang for their inestimable support.

I had the delight to conduct independent research while surrounded by exceptionally talented colleagues, both in my laboratory, clean rooms, and other departments. Specifically, I would like to acknowledge my long-time collaborator Yue (Jessica) Wang in Prof. Richard B. Kaner group. She is truly one of the brightest and most productive researchers I had the pleasure to work with. Dr. Francois Léonard and Dr. Aaron M. Katzenmeyer at Sandia National Laboratories provided unsurpassed capabilities for optoelectronic characterization at the nanoscale and I will always be thankful for that. I also owe my gratitude to Dr. Dieter Isheim at Northwestern University to introduce me with his decennial experience to one of the most exquisite atomic characterization techniques imaginable. I acknowledge the great help of Zhengliu Zhou and Abhejit Rajagopal who, at different times, contributed to theoretical simulations in the project. I express my appreciation to the Integrated System Nanofabrication Cleanroom and the Nanoelectronics Research Facility for thorough training and assistance.

Last, but definitely not least, I would like to warmly thank my family, my mother Franca, my father Gianni, and my sister Licia for being so close to me despite the distance. Their suggestions, love, and support over the years demonstrated to be extremely precious. I am the man that I am today as the product of your time and education.

Giacomo Mariani
November 2013
Los Angeles, CA

Vita

Education

2009-2013 *Graduate Student Researcher in Electrical Engineering*
University of California, Los Angeles, USA

2008-2009 *Staff Research Associate in Electrical Engineering*
University of California, Los Angeles, USA

2006-2008 *Master of Science in Electrical Engineering* (summa cum laude)
University of Bologna, Bologna, Italy

2003-2006 *Bachelor of Science in Electrical Engineering* (summa cum laude)
University of Bologna, Bologna, Italy

Selected publications

G. Mariani, Z. Zhou, A. Scofield, D. L. Huffaker "Direct-bandgap epitaxial core-multishell nanopillar photovoltaics featuring subwavelength optical concentrators", Nano Letters 13, 1632-1637 (2013)*

G. Mariani, A. Scofield, C.H. Hung, D.L. Huffaker "GaAs nanopillars-array solar cells employing in situ surface passivation", Nature Communications 4, 1497 (2013)*

G. Mariani, Y. Wang, P.-S. Wong, A. Lech, C.H., Hung, J. Shapiro, S. Prikhodko, M. El-Kady, R.B. Kaner, D.L. Huffaker "Three-dimensional core-shell hybrid solar cells via controlled in situ materials engineering", Nano Letters 12, 3581-3586 (2012)*

G. Mariani, P.-S. Wong, A.M. Katzenmeyer, F. Leonard, J. Shapiro, D.L. Huffaker "Patterned radial GaAs nanopillars solar cells", Nano Letters 11, 2490-2494 (2011)*

G. Mariani, R.B. Laghumavarapu, B. Tremolet de Villers, J. Shapiro, P.N. Senanayake, A. Lin, B.J. Schwartz, D.L. Huffaker "Hybrid conjugated polymer solar cells using patterned GaAs nanopillars", Appl. Phys. Lett. 97, 013107 (2010)*

G. Mariani, C. Tu, Z. Zhou, A. Scofield, J. Shapiro, D.L. Huffaker "Experimental matrix study of leakage current in nanopillar based devices towards high-efficiency photovoltaics", 39th IEEE Photovoltaic Specialists Conference, Tampa (2013)

G. Mariani, D. L. Huffaker "Direct-bandgap nanopillar photovoltaics based on patterned catalyst-free epitaxy", SPIE Invited Paper 8725, Micro- and Nanotechnology Sensors, Systems, and Applications V, 872510 (2013)*

G. Mariani, A. Scofield, D.L. Huffaker "High-performance patterned arrays of core-shell GaAs nanopillar solar cells with in situ InGaP passivation layer", 38th IEEE Photovoltaic Specialists Conference, Austin (2012)

G. Mariani, Y. Wang, P.-S. Wong, R.B. Kaner, D.L. Huffaker "Electrochemical polymerization of pedot on catalyst-free patterned GaAs nanopillars for high efficiency hybrid photovoltaics", 37th IEEE Photovoltaic Specialists Conference, Seattle (2011)

*Portions of this dissertation content have been drawn from these publications

Book Chapters

G. Mariani, Y. Wang, R.B. Kaner, D.L. Huffaker "Three-dimensional hybrid solar cells", Springer publisher

G. Mariani, D.L. Huffaker "Next-generation GaAs photovoltaics", Wiley publisher

Patents and Disclosures

G. Mariani (inventor) and D.L. Huffaker (non-inventor) "Subwavelength nanolens arrays as optical concentrators in nanowire photovoltaics" US 61/773,747

Honors, Awards, and Leadership

Fellowship Award for international *Exchange Abroad Program* (EAP), 2007/08

Nominated member of the *Minerals, Metals and Materials Society* (TMS)

Nominated mentor at *Leadership Excellence Accelerating potential* (LEAP) program

Honorable mention for "*2013 Franco Strazzabosco Young Engineer Award*" (presented on 10/29/13 in Washington DC)

Chapter 1

Introduction

1.1 Overview

Solar energy is the reason the human kind exists today and it is the main source of energy for all life forms. The amount of energy that the sun outputs every second is equivalent to ninety billion hydrogen bombs.[1] The sun has maintained this colossal power output for at least one billion years, and will continue to do so for several more billion years. While the majority of the current electricity production in the world is generated from fossil fuels such as natural gas, coal, and oil, these traditional power sources experience a number of difficulties including increasing prices, long-term availability, and growing climate change related to power generation using fossil fuels. Solar energy has emerged as one of the most rapidly growing renewable sources of electricity due to several advantages: *(1)* reduced dependence on fossil fuels, *(2)* limited impact on the environment, *(3)* matched peak time output with peak time demand, *(4)* extended modularity and scalability, and *(5)* flexible locations for installation at customer site.

The photon-to-electron process conversion occurs by means of solar cells. The advancements in the design and fabrication of photovoltaics can be categorized into three different generations of solar cells. The first generation includes large area silicon-based modules estimated to account for 86%[2] of the total photovoltaic market. However, mainly due to high manufacturing costs, a second generation of devices, thin-film solar cells, has been introduced to address low costs and high flexibility that permit integration on roof tops, solar shingles, etc. The

most cutting-edge technology is represented by the third generation of solar cells that completely replaces the standard paradigm of a two-dimensional (2D) planar p-n junction with new materials and novel three-dimensional (3D) design approaches. Polymer-based, nanostructure-based or dye-sensitized solar cells represent some of the innovative alternatives on which research teams are investing a considerable amount of time.

Crystalline silicon solar cells have recently achieved laboratory efficiencies of 25%,[3] requiring an inverted honeycomb texturing along with a rear local diffusion of dopants. The adjective 'crystalline' refers to the crystal growth phase during the preparation of the cylindrical semiconductor ingots. After oxygen, silicon (Si) is the most abundant element on Earth. Generally, silicon is obtained by the reduction of silicon dioxide (SiO_2) with carbon in an electric furnace from 1500 to 2000 °C. The silicon used in the semiconductor industry for the fabrication of devices is then further purified to bring impurity levels below the parts-per-billion level. In order to fabricate a silicon solar cell, a large, doped ingot is first sectioned into smaller ingots of proper size. Subsequently, each ingot is sliced and cleaned to yield a series of wafers. Phosphorus is then diffused into the semiconductor to constitute the second side of the photo-junction. Lastly, metal grid contacts are realized by screen-printing techniques. The non-optimized material usage and the multi-stepped fabrication involved are hindering the achievement of solar grid parity. A situation of grid parity occurs when a source of alternative power (e.g. solar) becomes cost competitive with standard sources (e.g. fossil fuel-based). In order to minimize the material usage and reduce the overall costs, new radical strategies to further slice the silicon wafers into thin films of semiconductors are being studied.

A first alternative approach to lower the cost of solar cells is represented by the development of conjugated polymers. One of the most important milestones was the introduction

of a C_{60} fullerene derivative to replace the conventional n-type polymers in organic solar cells.[4] In a typical organic device, donor and acceptor interfaces are intimately mixed together to constitute a bulk heterojunction. Such blends constitute the active absorber, able to harvest the photons and generate free charge carriers that can be collected at the electrodes. The mixture is in liquid form and can be promptly spin-coated on arbitrary substrates.[5] One of the main challenges is to unravel the complex selection of degradation phenomena that occurs in this type of optoelectronic devices. Photolytic and photochemical reactions are activated under illumination directly from the polymer, degrading the conversion efficiency over time in ambient atmosphere.[6] To date, the highest efficiency for this class of solar cells amounts to 10.6%.[7] Building efficient devices requires a systematic analysis of three different areas: materials design, morphology, and interface engineering. The total thickness for the light-harvesting active layer in solution processed photovoltaics is only a few hundred nanometers. This allows for low cost and flexible architectures, with processes compatible with roll-to-roll manufacturing for high volume production.

Another alternative solution to reduce manufacturing costs is to dramatically minimize the absorbing material usage with respect to planar photovoltaic configurations. Nanostructure-based solar cells integrate semiconductor layers with minimal thickness into lightweight, rugged solar cells that are flexible and adaptable to different surfaces.[8,9] The thickness range of such layers can vary from a few nanometers to several micrometers while ensuring ultra-high broadband solar photon absorption.[10]

1.2 Nanopillar Photovoltaics

Nanopillars (NP) are vertical arrays of semiconductor nanostructures. Their geometry accesses one additional spatial dimension compared to planar semiconductor films, therefore they are often referred to as 3D nanostructures.[11] NP photovoltaics represents a sustainable method to ensure high-efficiency solar power while reducing the manufacturing costs. Next-generation solar cells based on nanostructures have received increasing attention due to light trapping effects that dramatically increase the portion of absorbed photons while reducing the overall quantity of utilized semiconductor material. In periodically- and vertically-aligned arrays of NPs the incident optical field interacts with subwavelength structures in a completely different manner compared to planar architectures: while the NPs only cover a small percentage (5-15 %)[12] of the surface area, they exploit a principle known as resonant trapping to enhance the optical absorption by waveguiding light within the nanostructure as well as by recycling photons that bounce between adjacent NPs before being reflected back into the open space.[13,14] This situation is presented in Fig. 1.1.

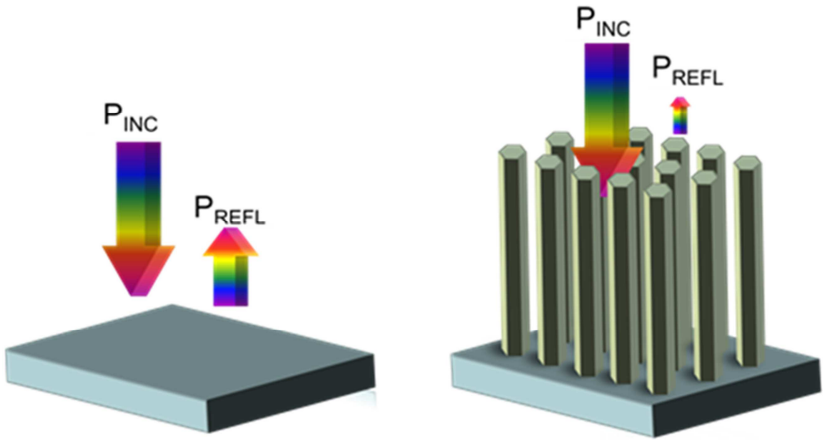

Figure 1.1. Comparative situation of light interaction with a planar semiconductor slab (left) and periodic NP array (right) of the same semiconductor material: resonant trapping occurring within each NP (i.e. light waveguide) and photon recycling taking place among neighboring NPs increases the probability of absorption of photons. Hence, the overall optical reflected power is dramatically reduced.

Light impinging onto a planar semiconductor slab is governed by the Snell's law and Beer-Lambert's absorption law.[15] With no anti-reflective coating or surface texturing, the portion of reflected light is simply determined by the refractive index mismatch at the boundary of the two materials as

$$R = \left(\frac{n_1 - n_2}{n_1 + n_2}\right)^2 \quad (1.1)$$

Equation (1.1) represents the reflection inherently arising from the refractive index mismatch of two media. For example, assuming the interface between air (n_{air} = 1) and GaAs (n_{GaAs} = 3.9), the reflection amounts to ~ 35%. This value can be reduced with anti-reflection coatings. Arrays of NPs are sequences of periodically-arranged subwavelength structures.

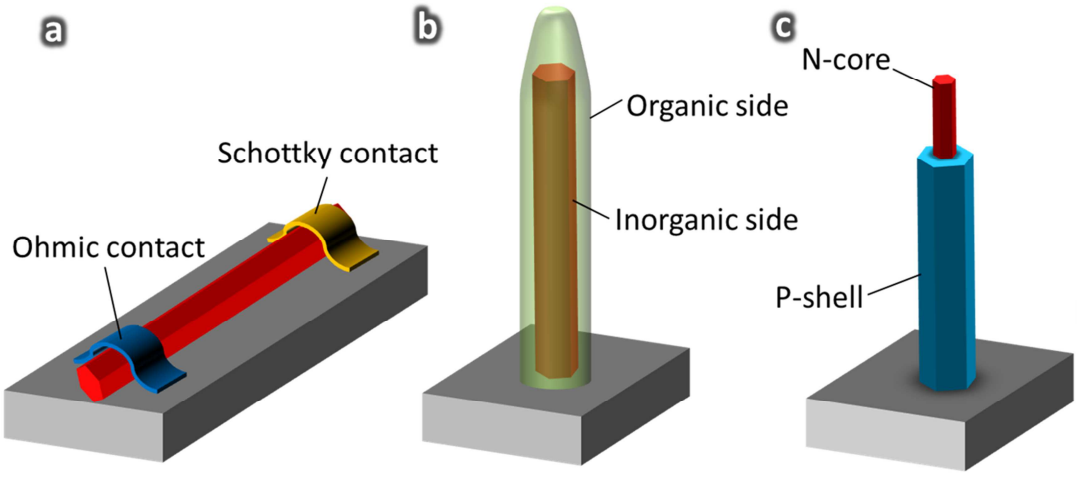

Figure 1.2. Schematic representations of a NP-based (a) Schottky junction, (b) organic-inorganic hybrid junction, and (c) all-semiconductor p-n junction.

In such framework of objects smaller than light wavelength, the interaction of optical field/NPs cannot be analyzed with the standard geometrical optics.[16] Full-wave simulations employing

Maxwell's equations (and not approximations) are necessary to rigorously model the light behavior once incident on NPs.[17]

An efficient optical absorption is the first step toward a high performing solar cell. Subsequent to photon absorption, the photo-generated carriers are separated at the electrical junction by means of a built-in electric field. The electrical junction can be implemented in the NP as a *(a)* Schottky junction,[18] *(b)* organic-inorganic hybrid junction,[19] and *(c)* all-semiconductor p-n junction.[20] The three categories of junction are schematically depicted in Fig. 1.2.

A Schottky junction solar cell is based on the interface between a metal and semiconductor that can induce a depletion or inversion layer in the semiconductor. A built-in potential defined as the Schottky barrier appears between the bulk of the semiconductor and the surface.[21]

An organic-inorganic hybrid junction solar cell combines conjugated polymers with inorganic nanostructures, with the intent of incorporating the advantages associated with both material groups. The inorganic electron donor material provides a more stable system in terms of chemical stability and photo-induced degradation, while offering a high-mobility channel to the photo-generated charge carriers.[22]

An all-semiconductor p-n junction solar cell exploits the direct incorporation of dopant atoms during the crystal formation to realize a fully-functional p-n (or p-i-n) diode. One of the greatest challenges is to control dopant intermixing and diffusion in the range of tens of nanometers to successfully embed the junction within each NP.[23] Besides, doping levels and gradients have to be finely controlled to establish an abrupt metallurgical junction. The electrical properties can be severely perturbed by surface states that be mitigate by different surface

passivation techniques. Transparent electrical contacts can form barriers and parasitic junctions that can block part of the charge carrier extraction to the external electrodes. This dissertation will focus on the two last types of junction.

1.3 Organization

This dissertation is divided into seven chapters. Chapter 1, the current chapter, sets the research framework of solar power, presents several emerging photovoltaic technologies that potentially can penetrate deeper into the current energy market, and succinctly outlines the dissertation. Chapter 2 introduces the concept behind organic-inorganic hybrid solar cell, the device structure, the material combination utilized, and the effect of ex-situ surface passivation on the properties of the active heterojunction. Chapter 3 addresses the controllability of the polymer deposition onto high-aspect-ratio vertical structures. Standard spin-casting dispensing is substituted by direct electropolymerization where polymer thickness, energy levels, and electrical conductivity can all be tuned in concert. Chapter 4 shifts gears and provides a second approach to NP photovoltaics that utilizes all-semiconductor p-n junctions embedded inside the nanostructures. The study is carried out as a comparison between two transparent conducting oxides sputter deposited onto the solar cell. The carrier extraction is found to be highly dependent on the Hall polarity of the electrode. Chapter 5 discusses the effect of lattice-matched epitaxial surface passivation as a tool to reduce the effect of native surface charge and states. The solar cell efficiency is maximized over six-fold with respect to a non-passivated device. Chapter 6 demonstrates enhanced open-circuit voltage by means of a passivated p-i-n radial junction. Full-wave electromagnetic modeling highlights an optical coupling tightly dependent on the morphology of the transparent top contact. A dome-shape electrode intensifies the photon field

inside the NP, while generating resonance peaks at fixed wavelengths that appear in external quantum efficiency measurements. Chapter 7 provides a brief summary of the research work performed and future outlook.

1.4 References

1. Naeye, R. Through the eyes of Hubble: the birth, life, and violent death of stars, Kalmbach Publishing Company (1998).

2. Wagner, L., Overview of the solar industry, Mora Associates research report (2007).

3. Green, M., Emery, K., Hishikawa, Y., Warta, W., Dunlop, E.D. Solar cell efficiency table (version 42), Prog. Photovolt: *Res. Appl.* **21**, 827-837 (2013).

4. O'Malley, K.M., Li, C.Z., Yip, H.L., Jen, A.K.Y. Enhanced open-circuit voltage in high performance polymer/fullerene bulk-heterojunction solar cells by cathode modification with a C_{60} surfactant, *Adv. En. Mat.* **2**, 82-86 (2012).

5. Gunes, S., Neugebauer, H., Sariciftci, N.S. Conjugated polymer-based organic solar cells, *Chem. Rev.* **107**, 1324-1338 (2007).

6. Jorgesen, M., Norrman, K., Krebs, F.C. Stability/degradation of polymer solar cells, *Sol. En. Mat. Sol. Cells* **92**, 686-714 (2008).

7. You, J.B., Dou, L.T., Yoshimura, K., Kato, T., Ohya, K., Moriarty, T., Emery, K., Chen, C.C., Gao, J., Li, G., Yang, Y. A polymer tandem solar cell with 10.6% power conversion efficiency, *Nat. Comm.* **4**, 1446 (2013).

8. Qi, J.F., Dang, X.N., Hammond, P.T., Belcher, A.M., Highly efficient plasmon-enhanced dye-sensitized solar cells through metal oxide core-shell nanostructure, *ACS Nano* **5**, 7108-7116 (2011).

9. Luther, J.M., Law, M., Beard, M.C., Song, Q., Reese, M.O., Ellingson, R.J., Nozik, A.J. Schottky solar cells based on colloidal nanocrystal films, *Nano Lett.* **8**, 3488-3492 (2008).

10. Ferry, V.E., Sweatlock, L.A., Pacifici, D., Atwater, H.A. Plasmonic nanostructure design for efficient light coupling into solar cells, *Nano Lett.* **8**, 4391-4397 (2008).

11. Mariani, G., Wong, P.-S., Katzenmeyer, A.M., Leonard, F., Shapiro, J., Huffaker, D.L. Patterned radial GaAs nanopillar solar cells, *Nano Lett.* **11**, 2490-2494 (2011).

12. Wallentin, J., Anttu, N., Asoli, D., Huffman, M., Aberg, I., Magnuss, M.H., Siefer, G., Fuss-Kailuweit, P., Dimroth, F., Witzingmann, B., Xu, H.Q., Samuelson, L., Deppert, K., Borgstrom, M.T. InP nanowire array solar cells achieving 13.8 % efficiency exceeding the ray optics limit, *Science* **339**, 1057-1060 (2013).

13. Mariani, G., Huffaker, D.L. Direct-bandgap nanopillar photovoltaics based on patterned catalyst-free epitaxy, *SPIE Invited Paper* 8725, Micro- and Nanotechnology Sensors, Systems, and Applications V, **872510** (2013).

14. Kelzenberg, M.D., Boettcher, S.W., Petykiewicz, J. A., Turner-Evans, D.B., Putnam, M. C., Warren, E.L., Spurgeon, J.M., Briggs, R.M., Lewis, N.S., Atwater, H.A. Enhanced absorption and carrier collection in Si wire arrays for photovoltaic applications, *Nat. Mat.* **9**, 239-244 (2010).

15. Kayes, B.M., Atwater, H.A., Lewis, N.S. Comparison of the device physics principles of planar and radial p-n junction nanorod solar cells, *Journ. Appl. Phys.* **97**, 114302-1-11 (2005).

16. Zhu, J., Yu, Z.F., Burkhard, G.F., Hsu, C.M., Connor, S.T., Xu, Y.Q., Wang, Q., McGehee, M., Fan, S.H., Cui, Y. Optical absorption enhancement in amorphous silicon nanowire and nanocone arrays, *Nano Lett.* **9**, 279-282 (2009).

17. Yao, J., Yang, X., Yin, X., Bartal, G., Zhang, X. Three-dimensional nanometer-scale optical cavities of indefinite medium, *PNAS* **108**, 11327-11331 (2011).

18. Ye, Y., Dai, Y., Dai, L., Shi, Z.J., Liu, N., Wang, F., Fu, L., Peng, R.M., Wen, X.N., Chen, Z.J., Liu, Z.F., Qin, G.G. High-performance single CdS nanowire (nanobelt) Schottky junction solar cells with Au/graphene Schottky electrodes, *ACS Appl. Mat. Int.* **2**, 3406-3410 (2010).

19. Briseno, A.L., Holcombe, T.W., Boukai, A.I., Garnett, E.C., Shelton, S.W., Frechet, J.J.M., Yang, P.D., Oligo- and polythiophene/ZnO hybrid nanowire solar cells, *Nano Lett.* **10**, 223-240 (2010).

20. Garnett, E.C., Yang P.D. Silicon nanowire radial p-n junction solar cells, *JACS* **130**, 9224 (2008).

21. Tersoff, J. *Phys. Rev. Lett.* **52**, 465-468 (1984).

22. McGehee, M.D. Nanostructured organic-inorganic hybrid solar cells, *MRS Bull.* **34**, 95-100 (2009).

23. Amit, I., Givan, U., Connell, J.G., Paul, D.F., Hammond, J.S., Lauhon, L.J., Rosenwaks, Y. Spatially resolved correlation of active and total doping concentrations in VLS grown nanowires, *Nano Lett.* **13**, 2598-2604 (2013).

Chapter 2

Hybrid solar cells employing spin-casting deposition

2.1 Overview

In the past few years polymer solar cells have gained attention due to their low cost, flexibility and ease of manufacturing.[1] Although conjugated polymers benefit from high absorption coefficients compared to inorganic semiconductors, low carrier mobilities (10^{-4} cm^2/Vs) limit their power conversion efficiency (*PCE*) to less than 11.1%.[2] In contrast, inorganic solar cells have high carrier mobilities, enabling effective charge extraction and thus high quantum efficiencies; with *PCE*s of 44.4%.[2] This suggests exciting possibilities for hybrid polymer/inorganic solar cells, which may be designed to simultaneously exploit the high carrier mobility from inorganic semiconductors and strong absorption coefficient from the polymer. Numerous hybrid devices have been demonstrated.

Common processing techniques for polymers, including spin-coating, inkjet printing, or doctor blading (only applicable to planar substrates) result in non-conformal coating or a thickness gradient when applied to three-dimensional structures. Hence, the reported hybrid solar cells are usually fabricated by either intimately mixing n-type inorganic nanostructures such as silicon nanocrystals,[3] cadmium selenide,[4] zinc oxide,[5] lead sulfide[6] or titanium dioxide[7] into the polymer prior to spin-coating, or infiltrate the polymer solution/dispersion into the 3D inorganic arrays to form an interdigitated block-like film. Both approaches diminish the purpose of having well-oriented, high mobility, 3D structured inorganic arrays that possess the unique advantage of directional charge transport and light trapping.

Aside from the device structure, the flexibly-tunable physical properties of the polymeric conductors by modern synthetic chemistry enable the optimization of the energy level alignment for organic and hybrid solar cells. Unfortunately, such desirable properties come at the price of extensive molecular engineering and intensive ad hoc synthesis, and the resulting polymers are often air-sensitive and need to be processed in glove-boxes. These structural and property limitations serve as the major hurdle in building a practical, highly efficient hybrid solar cell that can be potentially commercialized. Furthermore, coating a well-defined 3D inorganic semiconductor pattern, such as oriented nanowires, with an organic conductor allows for a high interface area and 3D features for the overall device, which is difficult to achieve with the all organic counterparts due to the lack of effective patterning techniques. As a result, materials development leading to inorganic and organic semiconductor/conductors with desired properties that can offer optimized morphology for charge transport and light harvesting is crucial and has become an expanding field of investigation. Surprisingly, relatively little work has been done involving hybrid solar cells with III-V inorganic nanostructures, despite the high efficiencies achieved in III-V bulk solar cells.

This chapter presents a type of hybrid inorganic/conjugated polymer photovoltaic device based on an array of patterned P3HT-coated n-GaAs NP heterojunctions. The corresponding schematic cartoon is shown in Fig. 2.1.

2.2 Fabrication of hybrid junction

The n-doped GaAs NPs are grown by selective area metal organic chemical vapor deposition (MOCVD) using a 300 Å SiO_2 mask evaporated onto a GaAs (111)B n^+-doped substrate. Multiple 1 cm^2 dies are patterned by e-beam lithography with 500 × 500 μm^2 patches on a 600 nm pitch. By using patterned growth rather than catalyzed, highly crystalline material free from residual Au-dopants is created, which results in very low leakage current.[8] Moreover, the highly regular geometric structure increases the optical path length by several times due to confinement of the optical rays in the nanostructured array, thereby enhancing the optical absorbance with respect to the bulk counterpart.[9] After the patterning, the samples are loaded into the MOCVD reactor.

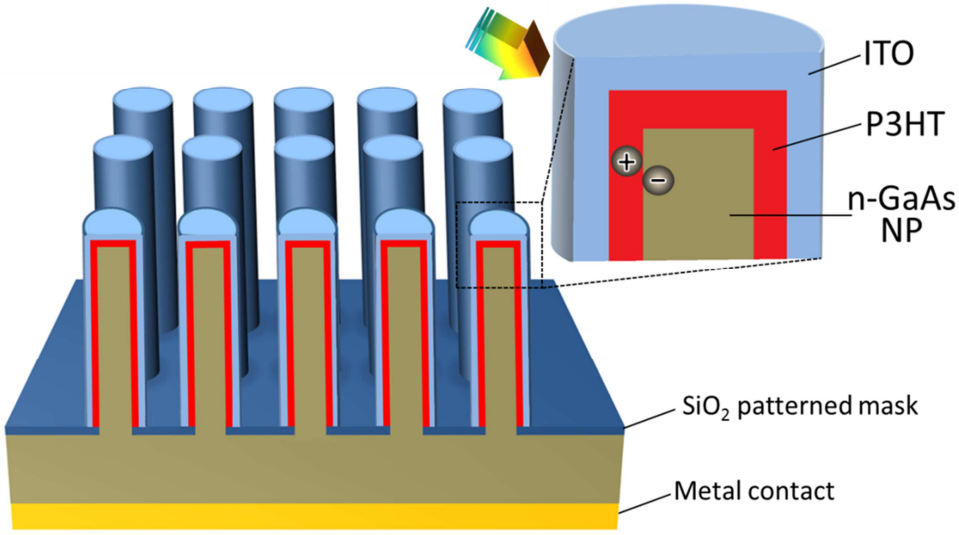

Figure 2.1. Schematic diagram of the GaAs/P3HT hybrid solar cell.

Trimethyl-gallium and tertiary-butyl-arsine source gases are flowed for 60 min with a V/III flux ratio of 8.5 and equivalent planar growth rate of 0.5 Å/s. Disilane is introduced to dope the pillars with a nominal doping concentration of 7 × 10^{18} cm^{-3} from previous thin-film

calibrations. Prior to any processing step, the samples are characterized by scanning electron microscopy (SEM), as shown in Fig. 2.2a. The average NP diameter and height are about 250 nm and 1.3 μm, respectively. An annealed AuGe/Ni/Au alloy forms the bottom ohmic contact. Prior to the polymer spin-coating, the samples are chemically treated in aqueous HCl (10 v/v%) solution at room temperature for 30 s to remove any native oxide on the pillar surface that could hinder the carrier extraction at the interface of the junction. The hybrid solar cells are prepared by spin-coating regioregular poly(3-hexylthiophene-2,5-diyl) (P3HT 90%-93%, Rieke Metal) from an o-dichlorobenzene solution onto the NP samples to produce a polymer film thickness of about 100 nm (as measured on flat substrate). The SEM image in Fig. 2.2b shows that P3HT clings uniformly to the base and sides of the pillars, with only a thin layer on top. To complete the devices, transparent indium tin oxide (SnO_2 / In_2O_3 10:90 wt%) (ITO) is RF sputtered at room temperature, providing an anode with an optical transmittance greater than 85% (range 400 nm < λ<1000 nm) nd a sheet resistance of 20 Ω/sq from planar calibrations.

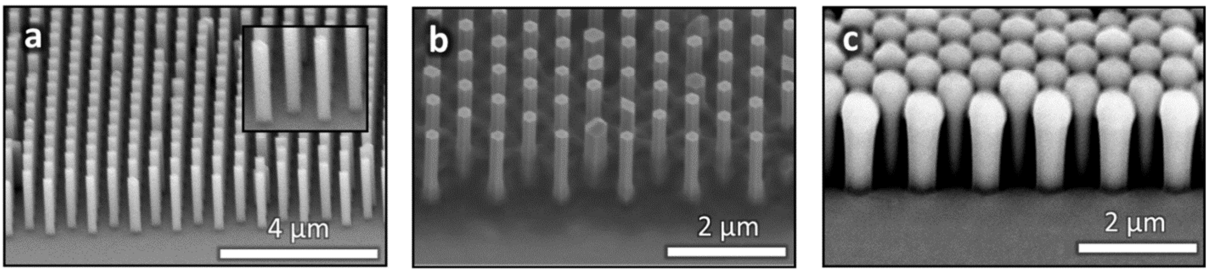

Figure 2.2. Cross-Sectional SEM of (a) an array of patterned n-doped GaAs NPs grown by MOCVD, (b) NP array after P3HT spin-coating, and (c) final hybrid device with ITO top contact.

Figure 2.2c shows that the sputtered ITO completely covers the NPs, forming a ball on top of each pillar. Control devices are also fabricated with the same NP growth, bottom contact

and ITO as a transparent front electrode, without any P3HT deposition, as well as control devices with P3HT spun on to the patterned-SiO_2 covered GaAs substrate without NPs.

2.3 Results and discussion

Figure 2.3 shows the *J-V* characteristics of the P3HT/GaAs hybrid solar cell, measured both in the dark and under AM1.5G (1 sun) illumination (1000 W/m^2). The active device area is 0.25 mm^2 and encompasses approximately 250,000 NPs. The device exhibits an open circuit voltage (V_{OC}) of 0.2 V, a short circuit current density (J_{SC}) of 8.7 mA/cm^2, and fill factor (*FF*) of 32%. The measured *PCE* is η = 0.6%. Under dark conditions, these devices exhibit very low leakage currents ($I_{leakage}$ = 110 nA @ -1 V), which it is attributed to extremely high crystallinity of the GaAs NPs and the high quality of the pillar/substrate interface. Furthermore, since the patterned NPs are grown catalyst free, they contain no residual dopants from catalyst material such as Au.

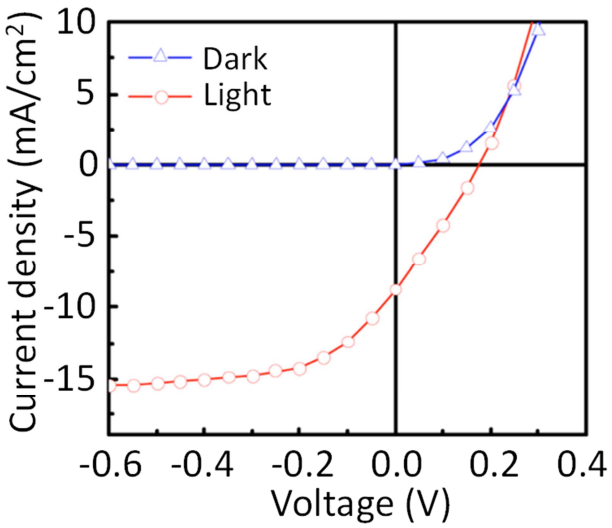

Figure 2.3. Current-voltage characteristics of the hybrid solar cell using P3HT and as-grown GaAs NPs (without ammonium sulfide passivation) under both dark conditions and AM1.5G (1 sun) illumination.

The overall performance of the hybrid solar cells demonstrated here are likely limited by several factors. The offset of the GaAs conduction band and the P3HT lowest unoccupied molecular orbital is large; although this helps encourage electrons from P3HT excitons to transfer into the GaAs conduction band, it also likely results in the observed low V_{OC}. Second, the presence of surface states on the GaAs NPs, caused by dangling bonds on the NP surface or by residual native oxide, are known to introduce nonradiative recombination sites, trap charges,[10] and pin the Fermi level to midgap. These effects can alter the effective doping concentration and deplete the NPs, reducing the size of their conducting channels.[11] Fortunately, it is known that chemical passivation can reduce both surface state density and surface recombination velocity.[12] Both theoretical[13] and experimental[14] analyses suggest that ammonium sulfide represents a suitable surface passivation agent, enhancing optical performance and eliminating the surface states on the NP facets.

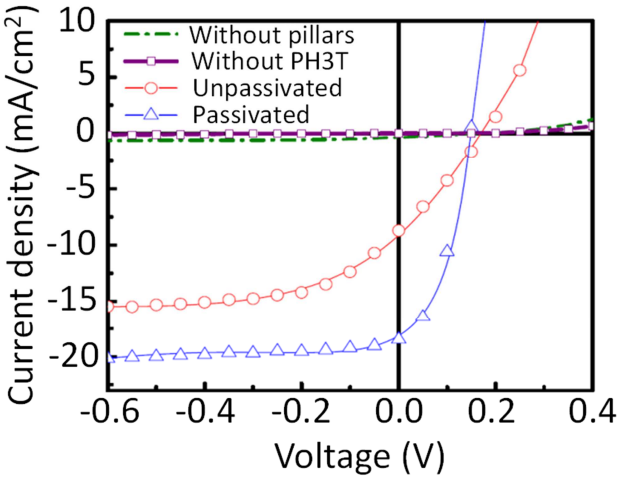

Figure 2.4. Comparison of *J-V* characteristics of the passivated and unpassivated hybrid solar cells along with a control cell without P3HT and another one without pillars. Measurements are carried out under AM1.5G (1 sun) illuminations.

Thus, a second set of hybrid devices is prepared in which the GaAs NPs are passivated in aqueous ammonium sulfide $(NH_4)_2S$ solution (22 v/v%) for 60 min at room temperature to

minimize the surface-state density. It is observed an equal extent of photoluminescence quenching for the passivated and nonpassivated samples, indicating that the passivation step did not significantly affect exciton harvesting. Figure 2.4 compares *J-V* characteristics of the hybrid cells with and without surface passivation (as well as the control cells without either any P3HT or any NPs). The samples that underwent passivation treatment exhibited a noticeable improvement in overall performance; despite a small reduction in V_{OC} (from 0.2 to 0.18 V), J_{SC} increases from 8.7 to 18.6 mA/cm^2 and the *FF* improves from 32% to 43%, resulting in a *PCE* of η = 1.44% with leakage current $I_{leakage}$ = 45 nA @ -1 V (under dark conditions).

Figure 2.5 shows the external quantum efficiency (*EQE*) data for passivated and unpassivated P3HT/GaAs hybrid solar cells.

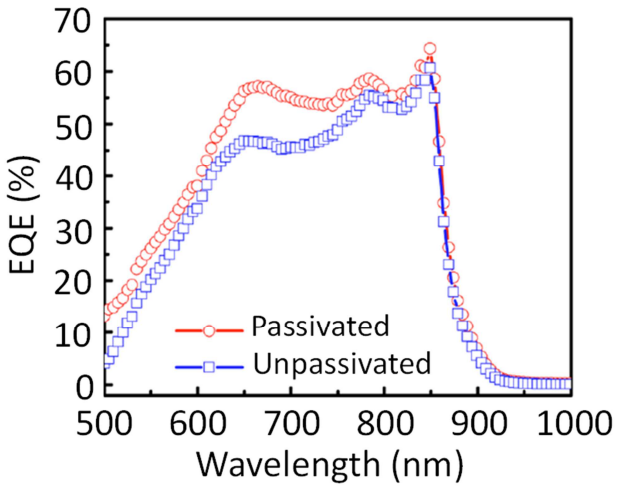

Figure 2.5. *EQE* measurements of passivated and unpassivated hybrid solar cells.

The contribution of P3HT[15] is visible in the left tail of the *EQE* plot, showing that absorption of light by the polymer (with absorption coefficient ~3×10^5 cm^{-1} @ λ = 500 nm) contributes to the photocurrent, despite the fact that the P3HT film is quite thin. Moreover, the absorption of GaAs

is also apparent throughout the entire *EQE* spectrum, showing that the hybrid device also has a significant fraction of photocurrent that results from absorption in GaAs and subsequent hole transfer to P3HT. The fact that absorption from both components contributes to the photocurrent provides a match with the solar spectrum that would be difficult to achieve with either component alone. Figure 2.5 also shows that surface passivation of the NPs increases the *EQE* across the entire absorption range; this indicates improved carrier collection, which most likely results from reduced trapping and/or recombination that occurs at surface defects on the GaAs NPs.

In summary, the study reports on a hybrid solar cell that combines n-doped GaAs NPs grown by catalyst-free MOCVD deposition and P3HT, a p-type semiconducting polymer. The PV device shows a promising *PCE* of η = 0.6%. Ammonium sulfide passivation improves the chemical and electronic properties of the nanostructure surface, resulting in an improved solar cell efficiency of η = 1.44%. A systematic and methodical study of these hybrid polymer/inorganic semiconductor interfaces will be crucial for the optimization of photon absorption, carrier collection/extraction and other phenomena that currently limit the overall *PCE* of solar cells.

2.4 References

1. Chen, L., Hong, Z., Li, G., Yang, Y. Recent progress in polymer solar cells: manipulation of polymer: fullerene morphology and the formation of efficient inverted polymer solar cells, *Adv. Mater*. **21**, 1434 (2009).

2. Green, M., Emery, K., Hishikawa, Y., Warta, W., Dunlop, E.D. Solar cell efficiency table (version 42), *Prog. Photovolt: Res. Appl.* **21**, 827-837 (2013).

3. Liu, C. Y., Zachary, C., Holman, U., Kortshagen, R. Hybrid Solar Cells from P3HT and silicon nanocrystals, *Nano Lett.* **9**, 449 (2009).

4. Zhou, Y., Riehle, F.S., Yuan, Y., Schleiermacher, H.F., Niggemann, M., Urban, G.A., Kruger, M. Improved efficiency of hybrid solar cells based on non-ligand-exchanged CdSe quantum dots and poly(3-hexylthiophene), *Appl. Phys. Lett.* **96**, 013304 (2010).

5. Huang, J., Yin, Z., Zheng, Q. Applications of ZnO in organic and hybrid solar cells, *Energy Environ. Sci.* **4**, 3861-3877 (2011).

6. Gunes, S., Fritz, K.P., Neugebauer, H., Sariciftci, N.S., Kumar, S., Scholes, G.D. Hybrid solar cells using PbS nanoparticles, *Sol. Energy Mat. Sol. Cells* **91**, 420-423 (2007).

7. Zhu, R., Jiang, C.Y., Liu, B., Ramakrishna, S. Highly efficient nanoporous TiO_2-olythiophene hybrid solar cells based on interfacial modification using a metal-free organic dye, *Adv. Mater.* **21**, 994-1000 (2009).

8. Ikejiri, K., Noborisaka, J., Hara, S., Motohisa, J., Fukui, T. Mechanism of catalyst-free growth of GaAs nanowires by selective area MOVPE, *Journ. Cryst. Growth* **298**, 616 (2007).

9. Pauzauskie, P.J., Radenovic, A., Trepagnier, E., Shroff, H., Yang, P., Liphardt, J. Optical trapping and integration of semiconductor nanowire assemblies in water, *Nat. Mater.* **5**, 97-101 (2006).

10. Schmidt, V., Senz, S., Gosele, U. Influence of the Si/SiO_2 interface on the charge carrier density of Si nanowires, *Appl. Phys. A: Mater. Sci. Process.* **86**, 187 (2006).

11. Björk, M.T., Schmid, H., Knoch, J., Riel, H., Riess, W. Donor deactivation in silicon nanostructures, *Nat. Nanotechnol.* **4**, 103 (2009).

12. Lebedev, M.V. Surface modification of III–V semiconductors: chemical processes and electronic properties, *Prog. Surf. Sci.* **70**, 153 (2002).

13. Ohno, T. Passivation of GaAs(001) surfaces by chalcogen atoms (S, Se and Te), *Surf. Sci.* **255**, 229 (1991).

14. Oigawa, H., Fan, J.F., Nannichi, Y., Sugahara, H., Oshima, M. Universal passivation effect of $(NH_4)_2S_X$ treatment on the surface of III-V compound semiconductors, *Jpn. J. Appl. Phys.* **30**, L322 (1991).

15. Shrotriya, V., Ouyang, J., Tseng, R.J., Li, G., Yang, Y. Absorption spectra modification in poly(3-hexylthiophene): methanofullerene blend thin films, *Chem. Phys. Lett.* **411**, 138 (2005).

Chapter 3

Hybrid solar cells via controlled in situ materials engineering

3.1 Overview

Mature materials engineering practices allow exquisite control of doping concentrations, band-offsets, and interface abruptness down to the atomic level. However, the most commonly polymers such as P3HT used in organic solar cells are often unstable in air and possess inferior transport properties. Major obstacles to advancing HSC device design have been the limited control over the organic layer features along with interfacial issues. Thus, a more sophisticated approach to materials engineering of hybrid solar cells (HSCs) remains an open challenge.

The hybrid interface represents the heart of any HSC devices. Tuning the energy levels in the polymeric conductor component for an optimal band arrangement is therefore one of the most important factors to rationally enhance the HSC performance potentially. By raising or lowering the energy levels or tuning the optical and electrical properties of the organic conductors, the band-to-band realignments between organic and inorganic layers can be altered, and thus maximizing the charge transfer and overall device efficiency. Such elegant materials engineering is typically achieved by modern synthetic chemistry.[1-3] However, applying the as-synthesized polymer to a 3D inorganic component such as nanowire arrays is challenging partly due to *(1)* the extremely specialized expertise required to prepare the functionalized polymers,

(2) the multistep synthesis/processing procedures, and *(3)* the lack of a reliable and reproducible method to produce conformal coatings over the vertical 3D inorganic structures.

In particular, common processing methods including spin-coating, inkjet printing, or doctor blading[4] used to apply the organic layer to inorganic nanostructures of silicon,[5] metal oxides,[6,7] II-VI compound semiconductors[8,9] or III-V nanowires[10] result in intimately mixed hybrid films or interdigitated, blocklike HSC active layers.[11,12] Using these techniques to coat individual vertical nanowires faces the challenge of non-conformal coatings or thickness gradients. Such coverage limitation diminishes the purpose of having well oriented, high mobility, inorganic arrays that possess both the advantages of directional charge transport and light trapping properties. Hence, these obstacles have hindered materials engineering from being exploited in hybrid photovoltaics.

This chapter discusses in details a new, simple approach that combines rapid polymerization directly and conformally onto the inorganic nanostructure surface, and in situ materials engineering to optimize the properties of the organic layer, such as the highest occupied molecular orbital (HOMO) energy levels and the conductivity, that eventually allows for the tuning of the interface properties and performance of 3D nanostructured core-shell HSCs. In brief, periodic GaAs NP arrays are fabricated via a fast, catalyst-free, bottom-up approach.[13] The GaAs NPs are coated with poly(3,4-ethylenedioxythiophene) (PEDOT) that is synthesized with different anionic dopants incorporated during an electrochemical deposition process in order to tailor its physical properties to better match the charge transfer/exchange with respect to the inorganic semiconductor counterpart.

3.2 Direct control of hybrid junction

The hybrid interface is explicitly tuned by *(1)* enhancing the in situ transport properties of PEDOT by using different dopant anions, *(2)* shifting the HOMO level of PEDOT downward to increase the V_{OC}, and *(3)* designing a PEDOT shell that balances out the short exciton diffusion length and the required thickness for light absorption. Furthermore, electropolymerization constitutes a low cost and selective technique that yields conformal radial shells around individual GaAs NPs to preserve the 3D features of the patterned array. A radial core-shell geometry is desirable because it allows for a shorter pathway for photogenerated carriers,[14,15] thereby enhancing the charge collection efficiency.

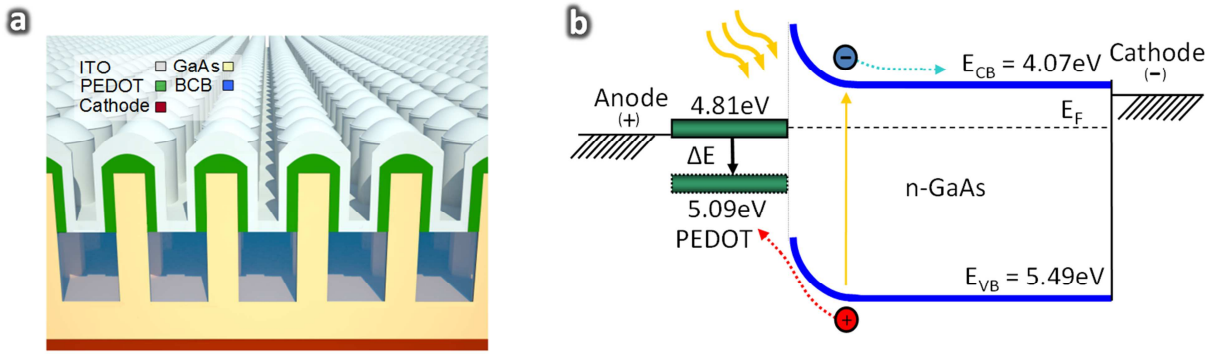

Figure 3.1. PEDOT/GaAs hybrid NP solar cells. (a) Cross-sectional schematic diagram of the hybrid NP solar cells as a 3D periodic array of core-shell inorganic-organic NPs. A GaAs NP periodic array is planarized after growth with BCB and then partly dry-etched back. Subsequently, the samples underwent electropolymerization of PEDOT by cyclic voltammetry (CV) in an EDOT monomer electrolyte solution, then ITO was RF sputtered to form the top transparent electrode. (b) Energy band diagram and alignment of the molecular orbital levels with respect to valence-conduction band edges, illustrating the independent photogenerated carrier flows.

Ensuring a conformal coating of well-defined 3D inorganic semiconductor patterns, such as oriented NPs, with an organic conductor allows for a large surface/interface area as well as enhanced absorption from nanostructuring, which is difficult to achieve for all-organic cells due to the current scarcity and limitations in their patterning techniques. In addition, the selected

conducting polymer here, PEDOT, unlike the readily photo-oxidizable P3HT,[16] is well known for its remarkable air stability,[17,18] which is essential for a practical device. Figure 3.1a-b illustrates the resulting device schematic and relevant energy levels in the hybrid device. As a first step, n-type GaAs NPs are grown on a masked n^+-GaAs substrate via selective area epitaxy (SAE). The growth is carried out using a MOCVD vertical-flow reactor with a hydrogen carrier gas at 60 Torr. The n-doped GaAs NPs are grown at 740 °C using tri-methyl-gallium (TMGa) and tertiary-butyl-arsine (TBA) as the primary precursors and tetra-ethyl-tin (TESn) as the dopant. The SAE is a catalyst-free alternative that does not introduce any contamination into the NPs,[19] and allows lithographic control of NP diameter, center-to-center pitch, tiling pattern, and periodicity.

3.2.1 Electropolymeric deposition of the organic layer

The process requires only a few minutes for growing a complete array of NPs. Several previous studies reported enhanced optical absorption[20,21] of NP arrays in comparison with planar architectures despite the low fraction of material utilized. Theoretical calculations (Lumerical FDTD Solutions) show that a 600 nm center-to-center pitch in a square lattice arrangement yields the maximum absorption.

Ohmic AuGe/Ni/Au (200 nm/40 nm/100 nm) back metal contacts on the as-grown NP arrays are electron-beam evaporated onto the dies and thermally annealed at 400 °C for 30 s. Subsequently, the samples undergo a 90 min surface passivation (22% $(NH_4)_2S$ aqueous solution (Alfa Aesar)) to mitigate the recombination effects introduced by surface states on the crystal facets. Ammonium sulfide is selected here as an excellent passivation agent for GaAs[22,23] in

which the sulfur-terminated GaAs NP surfaces interact with the sulfur on the EDOT monomer and lead to higher quality GaAs-PEDOT interfaces.

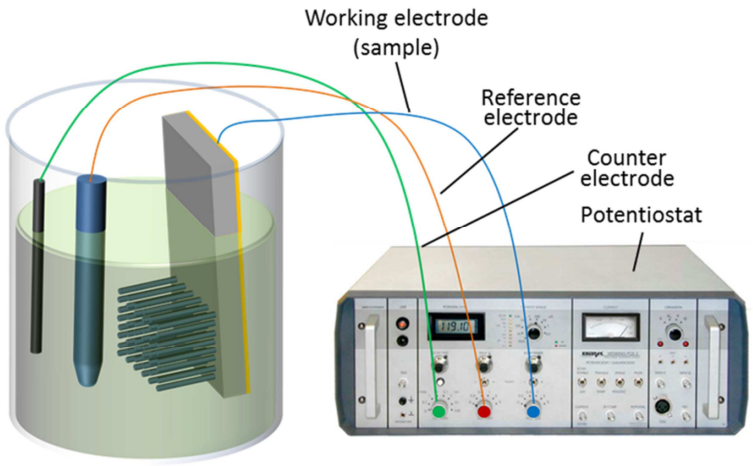

Figure 3.2. Electrodeposition setup composed of EDOT monomer solution, calomel reference electrode (orange), counter electrode (green), working electrode which biases the NP array, and potentiostat to implement the cyclic voltammetry.

Subsequently, benzocyclobutene (BCB) is spin-coated as an insulating resin onto the samples to prevent top-bottom shunting and then dry-etched back to expose only the top portion of the NPs. The patterned wafer is then immersed into an EDOT monomer solution with various electrolytes. Electropolymerization selectively grows PEDOT on the conductive GaAs while leaving the BCB layer intact, thus allowing for a highly controllable thickness and uniform radial coating. Electropolymerization is carried out under potentiodynamic conditions with potential applied by a VersaSTAT 3-400 potentiostat/galvanostat (Princeton Applied Research) using a standard one compartment, three-electrode setup with the GaAs NPs as the working electrode as depicted in Fig. 3.2.

Finally, indium tin oxide (ITO, Kurt J. Lesker) is deposited by RF magnetron sputtering as a top transparent electrode at a rate of 18 nm/min at room temperature at 5 mT of deposition pressure and 30 sccm of argon gas. Figure 3.1b depicts the band diagram of the final HSC.

PEDOT is a hole-injecting conducting polymer[24] and because of its positive temperature coefficient of resistivity, it manifests a metallic signature. For this reason, electrical conductivity is one of the main factors that affect the electronic transport of the photocarriers in the organic component of the junction.

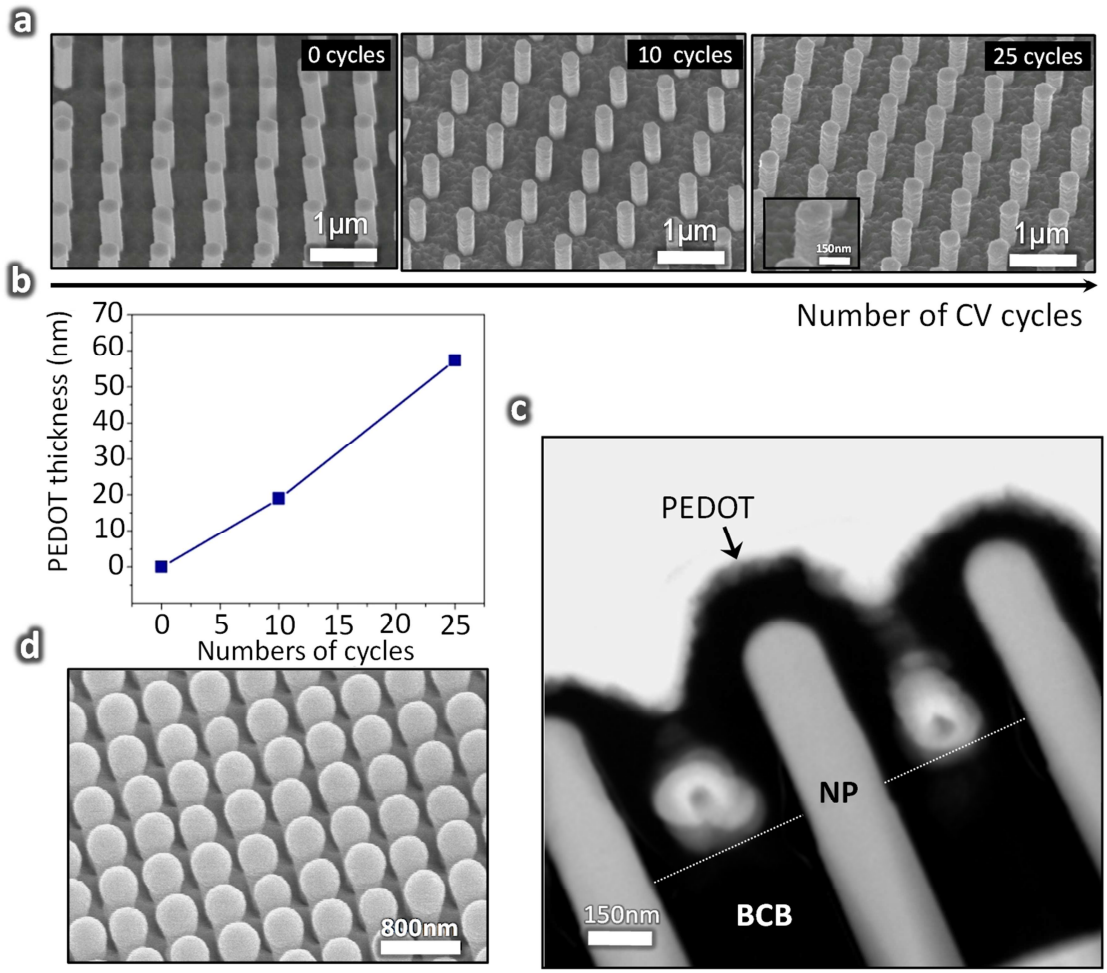

Figure 3.3. Nanoscale morphology control and TEM characterization.(a) SEM images of different stages of the electrodeposition applied to 190 nm diameter NPs, as a function of the number of CV cycles (constant center-to-center pitch of 600 nm). (b) Quasi-linear trends of PEDOT thickness with increasing number of CV cycles. (c) A cross-sectional TEM image showing complete conformal polymer coverage around the GaAs NPs. (d) An SEM image of the final device after ITO sputtering deposition. Note that the 3D morphology is preserved throughout all fabrication steps.

Upon illumination, the incoming photons generate electron-hole pairs in the GaAs layer, which then diffuse to the PEDOT/GaAs interface where they dissociate. Subsequently, free carriers (e^- and h^+) can travel to their respective electrodes to be collected. The charge diffusion process in the organic material is typically limited by the inherent short exciton diffusion length (5-30 nm),[25] so controlling the polymer thickness minimizes the distance from the hybrid interface.

In addition, the physical properties for the GaAs arrays such as NP diameter and doping concentration are kept constant to facilitate the investigation and comparison of different energy levels/conductivities of PEDOT on the device performance. Controlling the HOMO level of PEDOT is central to intimately correlate the physical properties of the polymer with that of the inorganic semiconductor at the active hybrid interface. Regarding the structural analysis of the electropolymerization, the deposition of PEDOT is evaluated in terms of thickness and coating morphology as a function of oxidation-reduction cycles applied to the GaAs NP arrays as shown in Fig. 3.3a-c. The arrays are standardized for equal center-to-center pitch (600 nm), height (~1.2 μm), and radius (190 nm). Figure 2a shows a collection of SEM images captured at the end of 0, 10, and 25 scanning cycles.

The thickness of the coating increases as a function of the number of cycles, as illustrated by the near linear trend shown in Fig. 2b, of 0, 20, and 55 nm, respectively. The deposition rate is pattern-dependent and related to the edge-to-edge distance among the NPs; stronger electric fields enable larger NPs to pull in a greater amount of EDOT monomers and dopant anions from the electrolyte, translating into a faster deposition rate. The average deposition rate calculated for 190 nm diameter NPs is ~24.0 Å/cycle. The nanometer precision is a crucial degree of freedom

for control of polymer thickness. Figure 3.3c shows a cross-sectional transmission electron microscope (TEM) image of hybrid NPs prepared by means of focused ion beam milling. The image confirms the high selectivity and uniformity of the organic coating (80 nm) of the exposed body of the GaAs NPs. A sputtered ITO anode (Fig. 3.3d) preserves the 3D morphology and completes the HSC fabrication. During electrodeposition, the negatively charged electrolyte anions bind to the positively charged PEDOT backbone, thus becoming part of the final polymer shell. This enables the analysis of several promising dopants for use in the GaAs-based structure.

3.2.2 Analysis of electrodeposited PEDOT: conductivity, dopants, and energy levels

Analysis of material composition, conductivity and HOMO levels are shown in Fig. 3.4 a-c.

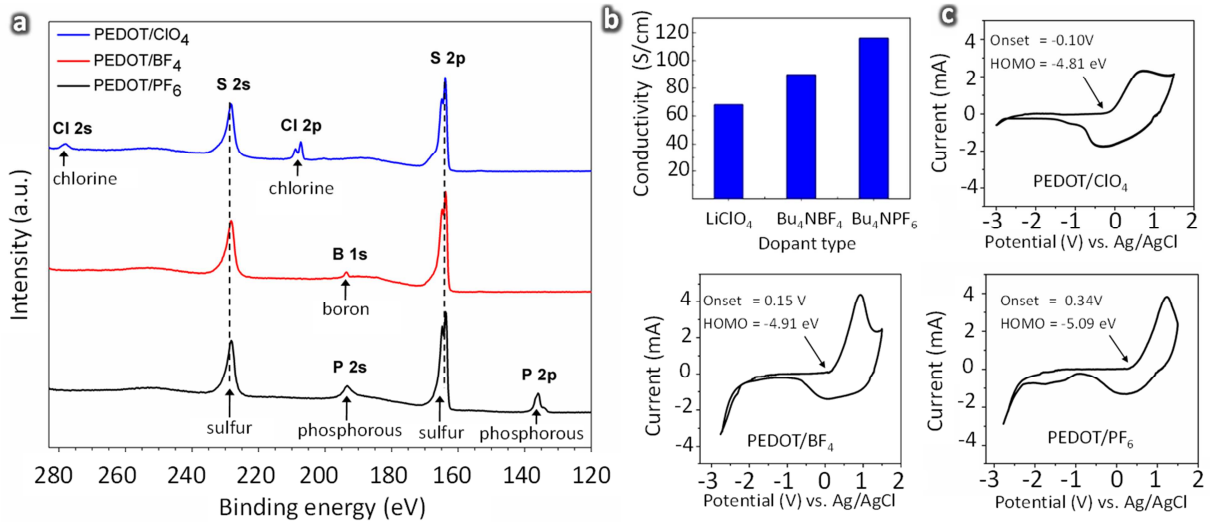

Figure 3.4. Polymer characterization with different dopant anions. (a) X-ray photoelectron spectroscopy of PEDOT synthesized with three different dopants: $LiClO_4$, Bu_4NBF_4, and Bu_4NPF_6. The elements chlorine, boron, and phosphorus from these three dopants can be identified respectively. (b) Electrical conductivity of PEDOT synthesized with the three different dopants, independently measured on Cr/Au-coated quartz slides along the vertical direction. (c) Cyclic voltammograms recorded for PEDOT synthesized with $LiClO_4$, Bu_4NBF_4, or Bu_4NPF_6.

Dopant incorporation is confirmed by X-ray photoelectron spectroscopy (XPS) (AXIS Ultra DLD, Kratos Analytical) as shown in Fig. 3.4a. The XPS also indicates a sulfur (S) elemental composition of 20% of oxidized sulfur (S^+) (peak area ratio of S^+ $2p_{3/2}$ to S $2p_{3/2}$),[26,27] suggesting a 20% doping concentration for all three kinds of dopant anions. Thus, one in every five EDOT monomers is oxidized regardless of the dopant type, resulting in an estimated hole concentration $n_p \sim 2 \times 10^{20}$ cm^{-3}. Figure 3.4b depicts the conductivity values with respect to different dopant incorporations into the PEDOT backbone. The general definition of conductivity σ for a p-type material is expressed in Eq. (3.1) as

$$\sigma = q(\mu_p n_p). \tag{3.1}$$

Consequently, increasing conductivities will result in easier percolation paths for the photogenerated charges to travel to the ITO anode. Five counteranions, PSS^- (poly-(styrenesulfonate)), DS^- (dodecyl sulfate), ClO_4^- (perchlorate), BF_4^- (tetrafluoroborate), and PF_6^- (hexafluorophosphate), are investigated as suitable dopants; however, only the last three were chosen for device testing since they resulted in the highest conductivities of approximately 68, 90, and 116 S/cm, respectively (Fig. 3.4b).

In order to characterize the band positions of the materials, cyclic voltammetry (CV) was utilized. CV for each polymer was carried out in a solution containing 0.1 M of the corresponding electrolyte salt that matches the dopant anion for each PEDOT, scanned at a rate of 0.05 V/s from -3.0 to 1.5 V. Figure 3.4c shows three different cyclic voltammograms corresponding to PEDOT/ClO_4, PEDOT/BF_4, and PEDOT/PF_6. All three types of PEDOT exhibit reversible oxidative p-doping processes in the positive potential regions, and a weak reductive behavior in the n-doping region when the reverse bias is applied. The oxidation

potential onsets are highlighted by arrows in the plots. Using a silver/silver chloride (Ag/AgCl) electrode in 3 M NaCl solution as reference potential, HOMO levels of -4.81, -4.91, and -5.09 eV, were calculated for PEDOT/ClO_4, PEDOT/BF_4, and PEDOT/PF_6, respectively. The most electronegative anions, PF_6^-, pull away the largest amount of electron density from the PEDOT backbone, significantly lowering the HOMO levels with respect to the GaAs band-edge.

3.3 Results and discussion

Figure 3.5a presents the measured *J-V* characteristics under 1-sun (AM1.5G) in ambient atmosphere.

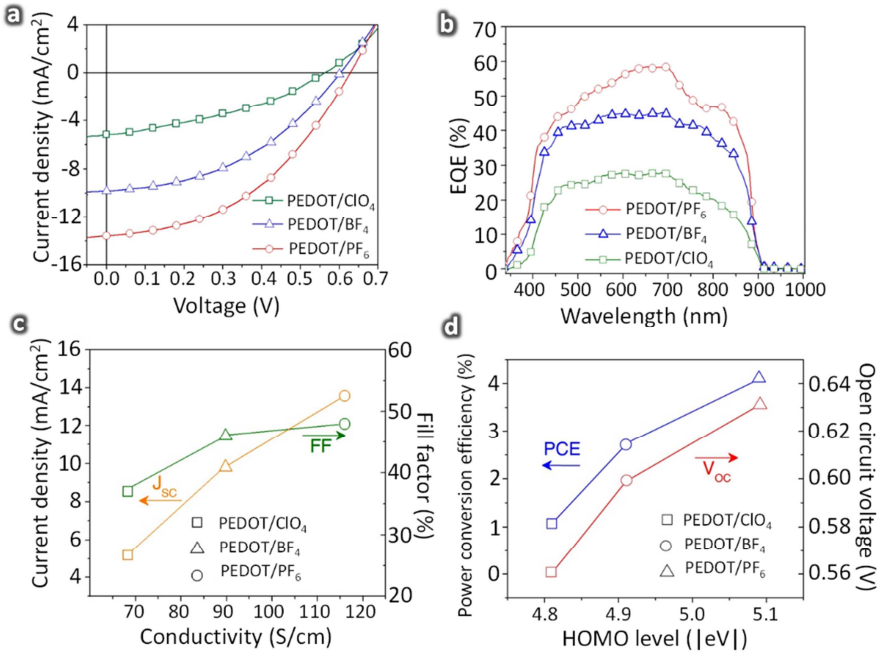

Figure 3.5. Electrical and electro-optical characterization of the hybrid NP solar cells. (a) *J-V* characteristics of hybrid photovoltaic arrays under illumination (1000 W/m^2) with differently doped PEDOT. (b) *EQE* measurements (from 340 to 1000 nm) for solar cells based on n-GaAs NPs processed with PEDOT/ClO_4, PEDOT/BF_4, and PEDOT/PF_6. (c) J_{SC} increases quasi-linearly with respect to the electrical conductivity of the polymer, whereas *FF* increases only slightly with an increase in conductivity. (d) V_{OC} increases by including different dopant anions and the *PCE* scales almost linearly with the polymer conductivity achieving peak values of 4.11%.

AM1.5G illumination is carried out with a 300 W xenon-lamp-based solar simulator (Newport Corporation, 67005) with an AM1.5G filter mounted. The light intensity is calibrated using a 1-sun (1000 W/m^2) reference silicon photodiode. A short circuit current density J_{SC} of 5.2 mA/cm^2 was obtained for the device with PEDOT/ClO_4 as the organic shell, whereas a J_{SC} of 9.8 and 13.6 mA/cm^2 are measured for the more conductive PEDOT/BF_4 and PEDOT/PF_6, respectively (Fig. 3.5a). Since the charge transport is directly related to the electrical properties of the polymer, enhancing the PEDOT conductivity by a simple change of dopant anion appears to be a feasible way to increase the current density step-by-step, which has been so far difficult to achieve in HSC.

Furthermore, since the ultimate V_{OC} $\left(\propto \frac{1}{q}|E_{CB} - E_{HOMO}|\right)$ is related to the energy level alignment between the p- and n-type materials, a lower HOMO level (E_{HOMO}) of the p-type polymer allows for a more favorable alignment with the conduction band edge (E_{CB}) of the n-type GaAs. Note that the downward tuning of the HOMO level enhances the V_{OC} value: the V_{OC} for the HSC with the PEDOT/ClO_4, PEDOT/BF_4, PEDOT/PF_6 organic shell is 0.56, 0.60, and 0.63 V, respectively, as the HOMO level of the polymer coating is lowered from -4.81, -4.91, and -5.09 eV (Fig. 3.5a). Hence, the incorporation of different dopant anions provides a simple way to deterministically increase the V_{OC} of the heterojunction. Figure 3.5b shows a comparison of the *EQE* spectra with respect to the three different doping schemes. The monochromatic illumination step is 5 nm and an objective lens with a focal length of 100 mm is used to focus down the spot size. The *EQE* shapes are overall quite similar with increasing

EQE values of ~27.9, 45.0, and 58.5% observed with increasing polymer conductivity, thus suggesting an optimum photocarrier balance between the electrons in the GaAs NP array

and the holes in the polymer. Hence, a successful engineering of the band energy of PEDOT results in improved charge separation at the polymer/GaAs interface, translating into higher J_{SC} and V_{OC}. The increased charge transfer at the interface is once again confirmed by the *EQE* spectra across the entire absorbing region. Figure 3.5c, along with Fig. 3.5d, summarizes the standard figures of merit for J_{SC}, *FF*, and V_{OC} required to calculate the total *PCE* ($V_{OC} \times J_{SC} \times FF / P_{AM1.5G}$). In Figure 3.5c, both J_{SC} and *FF* show increasing trends with respect to the polymer conductivity.

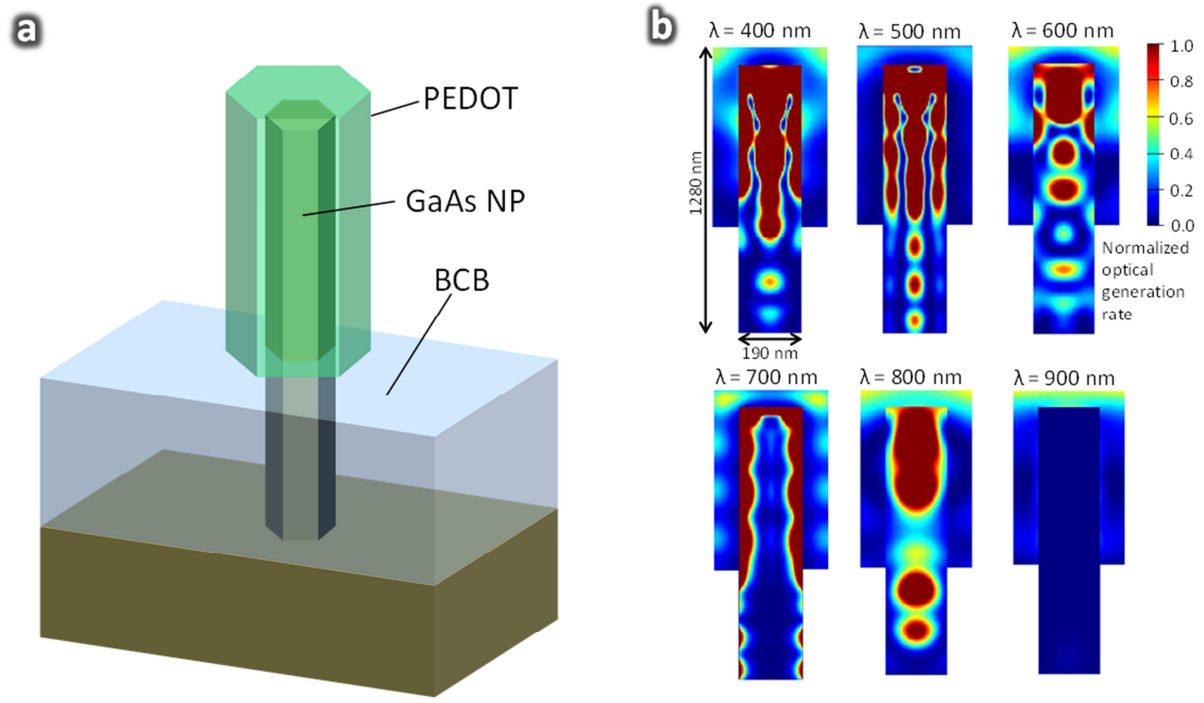

Figure 3.6. Spectral evolution of the photogeneration profile in a single hybrid NP. (a) Simulated structure for an individual hybrid core-shell NP. (b) Theoretical simulation of the carrier photogeneration profile at 400, 500, 600, 700, 800, and 900 nm. Up to λ = 800 nm, both organic and inorganic layers are optically active in the profile contribution.

Since the interface ITO/PEDOT is ohmic, the higher conductivity of the polymer lowers the specific series contact resistance, resulting in a higher *FF* of ~48% compared to previous polymer/GaAs nanowire (epitaxially grown) reports.[28] The overall *PCE* for the core-shell HSCs

monotonically increases from 1.07, 2.71, to 4.11% (Fig. 3.5d). The explicit, stepwise tuning of the figures of merit and the efficiencies of the devices illustrates the importance and the potential opportunities that materials engineering can bring to a HSC.

Representative 3D theoretical simulations (Lumerical FDTD Solutions) are carried out to correlate the *EQE* spectrum (Fig. 3.5b) with the photogeneration partitioned between the organic PEDOT shell and the inorganic GaAs core in the hybrid NP (Fig. 3.6a). Figure 3.6b illustrates the spectral evolution (2D cut-planes) of the photogeneration in the structure at different wavelengths varying from 400 to 900 nm for a 1.2 μm-high, 190 nm-diameter GaAs NP, with 80 nm of PEDOT shell. Because of delocalized orbitals in the doped PEDOT, the polymer is fairly optically active over the entire region of interest. However, the simulations consider 600 nm periodic boundary conditions to account for the enhanced absorption from an infinite array of NPs. Therefore, the optical field becomes highly confined within the nanostructure, as a result of the waveguiding and focusing of light[29] by the periodic array; the photogeneration rates are concentrated to several lobes that form along the NP, indicating strongly guided modes that arise from the nanostructuring of the 3D HSC. The simulations suggest that the final arraylike morphology still supports light-trapping effects. Above the bandgap (for λ = 900 nm), no optical generation is detected as confirmed from the EQE measurements.

In conclusion, this work demonstrates the importance of materials engineering for tuning the energy levels in the organic layer for optimizing the charge transfer at the hybrid interface. A facile electrodeposition approach is used as the delivering vehicle toward this goal by incorporating different anionic dopants in PEDOT and deterministically fabricate 3D hybrid core-shell PEDOT/GaAs pillars with a high degree of control over the radial thickness of the

organic shells. The electrodeposition technique allows for the rapid formation of PEDOT, conformal coating of the PEDOT around the oriented GaAs NP arrays, and the in situ engineering of the organic material properties in terms of feature size, thickness, conductivity, and energy levels. Adjusting the energy levels of PEDOT to more favorably align with the band structure of the inorganic semiconductor has led to the enhancement in the J_{SC}, V_{OC}, *EQE*, and the overall *PCE* of the final device, hence illustrating the great potential and the endless possibilities of molecular engineering via simple and rapid electrochemical synthesis.

3.4 References

1. Anthony, J. E. Functionalized acenes and heteroacenes for organic electronics, *Chem. Rev.* **106**, 5028-5048 (2006).

2. Briseno, A. L., Mannsfeld, S. C. B., Jenekhe, S. A., Bao, Z., Xia, Y. Introducing organic nanowire transistors, *Mater. Today* **11**, 38-47 (2008).

3. Liang, Y., Yu, L. A new class of semiconducting polymers for bulk heterojunction solar cells with exceptionally high performance, *Acc. Chem. Res.* **43**, 1227-1236 (2010).

4. Bandara, J., Willinger, K., Thelakkat, M. Multichromophore light harvesting in hybrid solar cells, *Phys. Chem. Chem. Phys.* **13**, 12906-12911 (2011).

5. Liu, C. Y., Zachary, C. H., Kortshagen, U. R. Hybrid solar cells from P3HT and silicon nanocrystals, *Nano Lett.* **9**, 449-452 (2009).

6. Beek, W. J. E., Wienk, M. M., Janssen, R. A. J. Hybrid solar cells from regioregular polythiophene and ZnO nanoparticles, *Adv. Func. Mat.* **16**, 1112-1116 (2006).

7. Moon, S. J., Baranoff, E., Zakeeruddin, S. M., Yeh, C. Y., Diau, E. W. G., Gratzel, M., Sivula, K. Enhanced light harvesting in mesoporous TiO_2/P3HT hybrid solar cells using porphyrin dye, *Chem. Commun.* **47**, 8244-8246 (2011).

8. Huynh, W. U., Dittmer, J. J., Alivisatos, A. P. Hybrid nanorod polymer solar cells, *Science* **295** (5564), 2425-2427 (2002).

9. Verma, D., Rao, A. R., Dutta, V. Surfactant-free CdTe nanoparticles mixed MEH-PPV hybrid solar cell deposited by spin coating technique, *Sol. Energy Mater. Sol. Cells* **93**, 1482-1487 (2009).

10. Ren, S., Zhao, N., Crawford, S. C., Tambe, M., Bulovic, V.,Gradecak, S. Heterojunction photovoltaics using GaAs nanowires and conjugated Polymers, *Nano Lett.* **11**, 408-413 (2011).

11. Baeten, L., Conings, B., Boyen, H. G., D'Haen, J., Hardy, A., D'Olieslaeger, M., Manca, J. V., Bael, M. K. V. Towards efficient hybrid solar cells based on fully polymer infiltrated ZnO nanorod arrays, *Adv. Mater*. **23**, 2802-2805 (2011).

12. Gunes, S., Sariciftci, N. S. Hybrid solar cells, *Inorg. Chim. Acta* **361**, 581-588 (2008).

13. Shapiro, J. N., Lin, A., Wong, P. S., Scofield, A. C., Tu, C., Senanayake, P. N., Mariani, G., Liang, B. L., Huffaker, D. L. InGaAs heterostructure formation in catalyst-free GaAs nanopillars by selective-area metal organic vapor phase epitaxy, *Appl. Phys. Lett.* **97**, 243102 (2010).

14. Tian, B., Kempa, J. T., Lieber, C. M. Single nanowire photovoltaics, *Chem. Soc. Rev.* **38**, 16-24 (2009).

15. Mariani, G., Wong, P. S., Katzenmeyer, A. M., Leonard, F., Shapiro, J., Huffaker, D. L. Patterned radial GaAs nanopillar solar cells, *Nano Lett.* **11**, 2490-2494 (2011).

16. Hintz, H., Egelhaaf, H. J., Lüer, L., Hauch, J., Peisert, H., Chassé, T. Photodegradation of P3HT - A systematic study of environmental factors, *Chem. Mater*. **23**, 145-154 (2011).

17. Andreas Elschner, A., Kirchmeyer, S., Lovenich, W., Merker, U., Reuter, K. PEDOT: principles and applications of an intrinsically conductive polymer, *CRC Press: Boca Raton*, FL, (2011).

18. Martin, D. C., Wu, J., Shaw, C. M., King, Z., Spanninga, S. A., Richardson-Burns, S., Hendricks, J., Yang, J. The morphology of poly(3,4-ethylenedioxythiophene), *Polym. Rev.* **50**, 340-384 (2010).

19. Lin, A., Shapiro, J. N., Senanayake, P. N., Scofield, A. C., Wong, P. S., Liang, B., Huffaker, D. L. Extracting transport parameters in GaAs nanopillars grown by selective-area epitaxy, *Nanotechnology* **23**, 105701 (2012).

20. Kelzenberg, M. D., Boettcher, S. W., Petykiewicz, J. A., Turner-Evans, D. B., Putnam, M. C., Warren, E. L., Spurgeon, J. L., Briggs, R. M., Lewis, N. S., Atwater, H. A. Enhanced absorption and carrier collection in Si wire arrays for photovoltaic applications, *Nat. Mater.* **9**, 239-244 (2010).

21. Zhu, J., Yu, Z., Burkhard, G. F., Hsu, C.-M., Connor, S. T., Xu, Y., Wang, Q., McGehee, M., Fan, S., Cui, Y. Optical absorption enhancement in amorphous silicon nanowire and nanocone arrays, *Nano Lett.* **9**, 279-282 (2009).

22. Yablonovich, E., Skromme, B. J., Bath, R.; Harbison, J. P., Gmitter, T. J. Band bending, Fermi level pinning, and surface fixed charge on chemically prepared GaAs surfaces, *Appl. Phys. Lett.* **54**, 555-557 (1989).

23. Takahisa, O. Sulfur passivation of GaAs surfaces, *Phys. Rev. B* **44**, 12 (1991).

24. Ohshita, J., Tada, Y., Kunai, A., Harima, Y., Kunugi, Y. Hole injection properties of annealed polythiophene films to replace PEDOT-PSS in multilayered OLED systems, *Synth. Mater*. **159**, 214-217 (2009).

25. Qin, D., Gu, P., Dhar, R. S., Razavipour, S. G., Ban, D. Measuring the exciton diffusion length of C_{60} in organic planar heterojunction solar cells, *Phys. Status Solidi A* **208**, 1967-1971 (2011).

26. Spanninga, S. A., Martin, D. C., Chen, Z. X-ray photoelectron spectroscopy study of counterion incorporation in poly(3,4-ethylenedioxythiophene), *J. Phys. Chem. C* **113**, 5585−5592 (2009).

27. Spanninga, S. A., Martin, D. C., Chen, Z. X-ray Photoelectron Spectroscopy study of counterion Incorporation in poly(3,4-ethylenedioxythiophene) (PEDOT) 2: polyanion effect, toluenesulfonate, and small anions, *J. Phys. Chem. C* **114**, 14992−14997 (2010).

28. Bi, H., LaPierre, R. R. A GaAs nanowire/P3HT hybrid photovoltaic device, *Nanotechnology* **20**, 465205 (2009).

29. Kelzenberg, M. D., Putnam, M. C., Turner-Evans, D. B., Lewis, N. S.; Atwater, H. A. Predicted efficiency of Si wire array solar cells, *34th IEEE Phot. Spec. Conf.* 391−396 (2009).

Chapter 4

Radial GaAs nanopillar solar cells

4.1 Overview

Nanostructured solar cells have gained much attention due to light trapping effects that drastically reduce the portion of reflected photons, therefore enhancing the optical absorption. Nanodomes,[1] nanocones,[2] nanoparticles,[3] and nanowires[4,5] (NWs) have the potential to improve performance compared to standard solar cells. The high surface-to-volume ratio increases the photoactive junction area and facilitates the carrier collection, enhancing the *PCE* with respect to bulk solar cells. In particular, compared to top-down[6] approaches, a bottom-up growth mode may lead to high-quality composition, crucial for any photovoltaic device. Furthermore, by exploiting radial junctions in each single NW, the light absorption (vertical direction) is decoupled from the carrier collection (radial direction), an unresolved issue in conventional planar solar cells.

Recently, silicon microwire solar cells[7] grown as ordered arrays have achieved *PCE* of 7.9%. However, due to the low optical absorption coefficient of silicon, long nanowires (~60 μm) are required to absorb the above-band-gap photons. III-V, direct band gap technology requires ~1 μm of material to efficiently absorb the photons and integration of radial multijunctions becomes possible too. In addition, GaAs crystalline single junction solar cells[8] have recently demonstrated the highest *PCE* (up to 28.8%) in monojunction photovoltaics. Despite that, only one reported work regarding radial GaAs nanostructures,[9] based on Au-catalyzed vapor-liquid-solid (VLS) growth, demonstrates core-shell NW growth for photovoltaic

applications. These photovoltaic devices exhibit low *PCE*s (0.83%), possibly due to the random distribution in terms of height, diameter, and position. Furthermore, the midgap trap states introduced by diffusion of Au catalyst into the NW[10] degrade minority carrier lifetime and diffusion length on which photovoltaic devices rely.

For successful devices, NW diameter, length, and filling ratio have to be carefully chosen and kept constant by the adoption of a regular geometry.[11] The less semiconductor material required to absorb the same amount of photons with respect to thin films in conjunction with the possibility to peel off the NWs from the substrate and reuse it in subsequent growths opens up promising routes to low-cost, flexible solar cells. One approach to realizing a patterned architecture is to take advantage of lithographic techniques to precisely define radius and center-to-center pitch in a mask from which the NWs can be grown. Such a mask translates into a uniform NW growth, allowing ease of processing/fabrication and avoiding adjacent NW junctions from contacting each other during growth. In addition, the small NW cross sections that can be realized allow the growth of junctions of dissimilar materials with high lattice-constant mismatch, permitting a prompt integration of heterogeneous material platforms.

Device structure and geometry, nonetheless, are not sufficient to ensure high-efficiency nanostructured photovoltaics: each interface must be carefully designed, including the nature of the contacts. This is especially true for degenerately doped semiconducting oxides such as ITO or aluminum zinc oxide (AZO). Their properties can profoundly modify carrier extraction/injection mechanisms once they come into contact with p-doped and n-doped semiconductors.

This chapter discusses in detail the performance, in terms of electrical and electro-optical properties, of GaAs NP solar cells based on a patterned periodic geometry. The devices are processed using with two transparent conducting oxides (TCO) to assess the most appropriate contact scheme.

4.2 Patterning and processing of radial junction devices

The device schematic and fabrication scheme are shown in Fig. 4.1. The core-shell NPs are formed by catalyst-free, selective-area MOCVD. A 25 nm thick SiO_2 mask is deposited by e-beam evaporation on a p-doped (111)B GaAs substrate and patterned using e-beam lithography and reactive-ion etching to have 500 μm × 500 μm arrays of holes with 600 nm spacing (0.25 mm^2 device area). The p-doped core is formed at a temperature of 685 °C for 15 min resulting in diameters of ~ 200 nm and heights of ~ 800 nm whereas the n-doped shell is grown at a reduced temperature of 665 °C for 2.5 min resulting in final diameters of 320 nm and heights of 900 nm. Disilane and diethyl zinc flow rates are chosen to produce carrier densities of $N_D = 1 \times 10^{18}$ cm^{-3} and $N_A = 3 \times 10^{17}$ cm^{-3}, calibrated on thin GaAs films. Figure 1a shows the schematic of the fabricated devices. Figure 4.1b illustrates a 45°-tilt SEM image of the as-grown NP array with built-in radial p-n junctions grown in situ.

The hexagonal faceting suggests a good crystal growth quality. As aforementioned, the expected p-doped core diameter is ~200 nm whereas the n-doped surrounding shell is estimated to be ~60 nm wide.

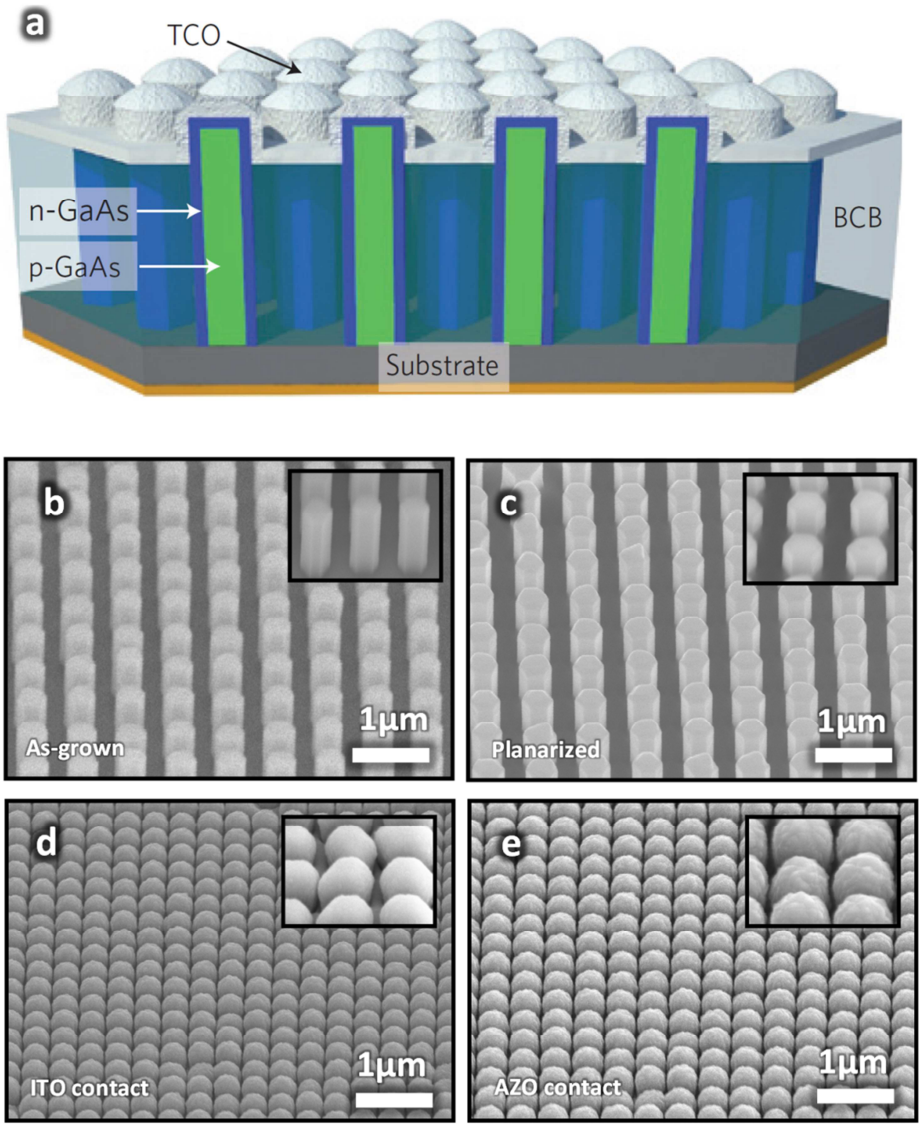

Figure 4.1. (a) Schematic drawing of the ordered GaAs NP solar cell. (b) 45°-tilt SEM image of an array of GaAs NPs with built-in radial p-n junctions. (c) 45°-tilt SEM image after BCB planarization and dry etchback to expose only the NP tips. (d) 45°-tilt SEM image subsequent to ITO sputtering and relative coating of the NP tips. (e) 45°-tilt SEM image after AZO deposition on NP tips.

Due to the nanometer level dimensions, both highly doped core and shell are required in order to confine the depletion region well within the NW: a quasi-neutral core region is required in order for the carriers to travel all the way to the substrate and bottom electrode. Considering doping levels from planar calibrations, the total estimated depletion width in the NP amounts to

~90 nm, ensuring quasi-neutral regions on both core and shell sides. The device processing flow is initiated by a chemical treatment of the as-grown NP arrays in aqueous hydrochloric acid (HCl, 10% v/v) solution for 45 s to remove any native oxide on the surface followed by chemical passivation by means of ammonium sulfide $(NH_4)_2S$ solution (22% v/v) for 90 min to minimize the surface-state density.[12]

Interface states, in fact, are likely to misbalance the electric fields and depletion regions at the nanometer scale, translating into poor or unpredicted behaviors in junction-based devices. After that, BCB resin (Cyclotene, Dow Chemical) is spun to completely cover the NP arrays in transparent electrical insulator. Subsequent to BCB hard-curing, the excess resin is removed by an O_2/CF_4 reactive ion etching to expose only the NP tips. Lastly, TCO (ITO (SnO_2:In_2O_3 10:90 wt%) or AZO (Al_2O_3:ZnO 2:98 wt%)) is deposited as top electrode. Bottom ohmic contacts to the heavily doped substrate are formed by a Ti/Au (30 nm/200 nm) alloy. As shown in Fig. 4.1c, the exposure of the NP tips after plasma etching is 250 nm, leaving two-thirds of the nanostructures encapsulated in the BCB polymer.

Subsequently, ITO or AZO are RF sputtered at room temperature at 200 W of applied RF power and 5 mT deposition pressure. These deposition parameters are found to be the optimum conditions for highly conductive and transmitting films. Figure 4.1d indicates that the deposition of ITO onto the NP array provides a conformal top contact across the NP tips. Figure 4.1e displays the SEM micrograph for the AZO sputtered contact on the device. AZO appears to have a more textured surface compared to ITO, suggesting a bigger average grain size. However, due to the final shape of the NP tips after deposition, light trapping is still expected due to the presence of gaps between adjacent NPs for both ITO and AZO.

4.2.1 Structural and morphological analysis of contacts

The structural and morphological qualities of the TCOs are analyzed by cross-sectional transmission electron microscopy (TEM) images. Figure 4.2a shows a cross-sectional TEM image, sectioned by means of focused ion beam milling. The image reveals the ITO electrode in contact with a GaAs core-shell NP.

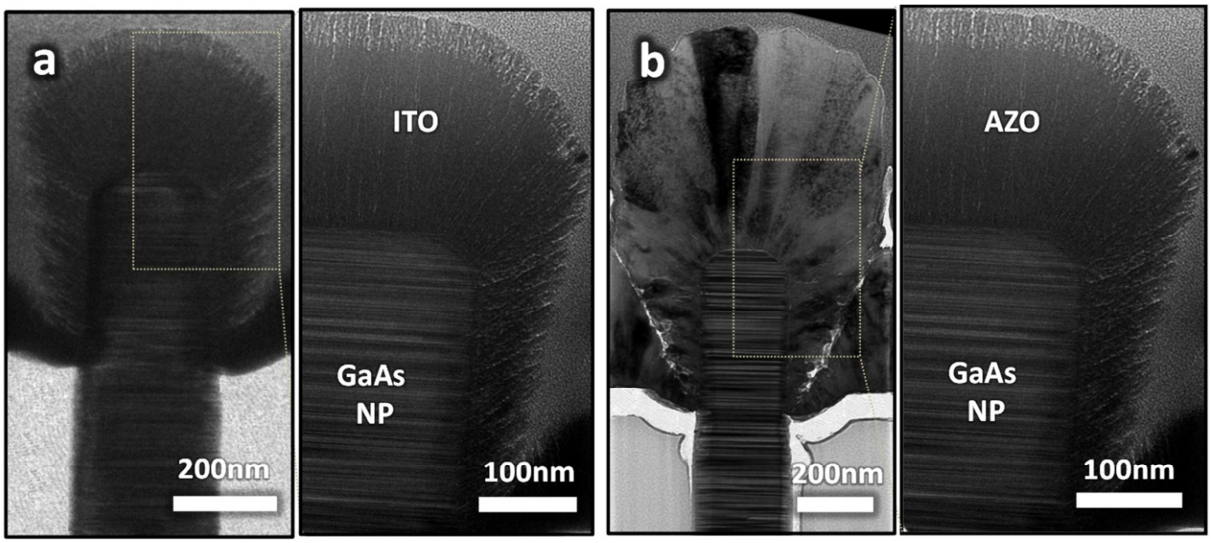

Figure 4.2. (a) Cross-sectional transmission electron microscope (TEM) image of a NP with ITO as top electrode and BCB as surrounding insulator. (b) Cross-sectional TEM image of a NP with AZO as top transparent contact.

The TCO is uniform in quality along the whole NP tip. Electron diffraction patterns taken during TEM (not included here) confirm the amorphous nature of the thin film. This is in agreement with previous works regarding ITO RF sputtered at room temperature: substrate temperatures[13] in excess of ~200 °C are required to achieve a crystalline version of the material. The ITO thickness reduces at the bottom edges of the NP/BCB interface due to shadowing

effects that decrease the deposition rate of ITO. However, the film remains continuous with a thinnest layer of around 60 nm. Figure 2b displays a cross-sectional TEM of AZO contact deposited on top of the same NP structure. The AZO thin film appears thicker with respect to ITO due to the fact that the actual deposition rate on NPs is higher for the AZO target, even though the deposition conditions (sputtering power, substrate temperature, deposition time, pressure) are kept constant for both cases. Structurally, the AZO exhibits defects such as grain boundaries that can contribute to an increase in film resistivity. The conformation of AZO suggests a polycrystalline structure. This hypothesis is confirmed by electron diffraction patterns analyzed during TEM (not included here).

4.3 Results and discussion

To characterize and compare the electrical properties of the devices based on these two different transparent top contacts, *J-V* characteristics are measured both in dark conditions and under AM1.5G normal illumination (1000 W/m^2, 1 sun) at room temperature. Also, *EQE*

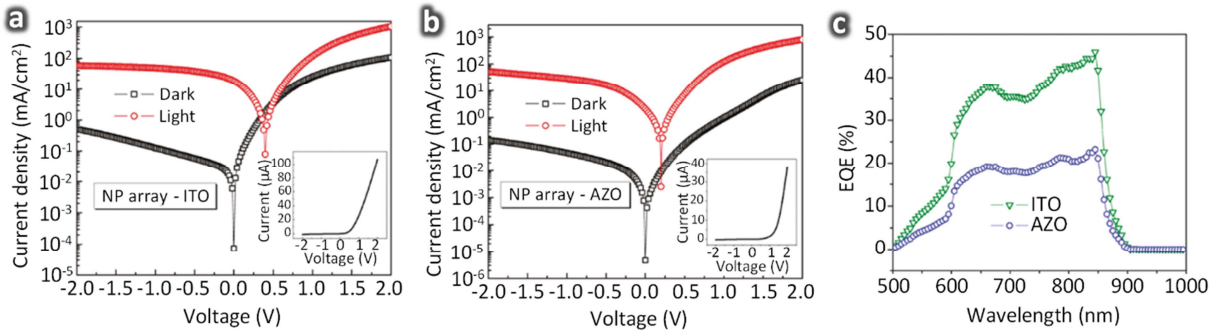

Figure 4.3. (a) *J-V* characteristic for the best NP solar cell with ITO as top contact both in the dark and under AM1.5G illumination. The inset shows the IV characteristic in linear scale for the device in the dark. (b) *J-V* characteristics of the best NP solar cell with AZO as top electrode both in the dark and under AM1.5G illumination. The inset shows the *I-V* characteristic in linear scale for the device in the dark. (c) *EQE* measurements of NP solar cells processed with ITO and AZO top contacts.

measurements are carried out to analyze the normalized distribution of the photocurrent along the visible spectrum of interest (from ~500 to 900 nm for GaAs).

Figure 4.3a shows *J-V* characteristics both in the dark and under light. The inset illustrates, on a linear scale, the current-voltage (*I-V)* characteristic of the sample with ITO as top contact: a high rectification ratio of 213 (@ ± 1 V) is achieved. Leakage currents in the order of ~236 nA at -1 V are measured. The values of rectification ratio and leakage current attributed to the regularity of the catalyst-free patterned growth (it eliminates parasitic shunting paths between adjacent NPs likely to occur in VLS-based arrays) and to the uniform BCB passivation/planarization layer. Under light, the device exhibits a V_{OC} of 0.39 V, and a J_{SC} of 17.6 mA/cm^2 with a *FF* of 37% resulting in a total *PCE* of 2.54%. Figure 4.3b presents *J-V* characteristics for a NP array with AZO as top electrode. Once again, the linear inset shows a good diode behavior of the junction in dark conditions with a rectification ratio of 183 (at ± 1 V) and leakage currents of ~ 170 nA at -1 V.

Upon illumination, the photovoltaic conversion results in a V_{OC} = 0.2 V, J_{SC} = 8.1 mA/cm^2, *FF* = 36% with a *PCE* = 0.58%. The planarization process is crucial in order to avoid undesired conduction between the top contact and the substrate that could reduce or annul the rectification action of the NPs. Furthermore, BCB has extensively been shown to additionally passivate GaAs devices, lessening the reverse leakage currents.[14,15] This also aids, for the ITO device, in enhanced V_{OC} (0.39 V) compared to 0.2 V previously reported in radial GaAs NW photovoltaics. The relatively low values of *FF* in both cases can be partly attributed to the presence of a non-negligible series resistance in the devices.

Considering that the bottom electrodes are realized by well-established low-resistance alloys, the top electrodes (ITO and AZO) are causing a significant increase in the series resistance of the NP arrays, translating into low *FF*. From panels a and b of Fig. 4.2 it can be noticed that the deposition of the oxides forms a thin layer at the interface NP tip/BCB, likely to cause a bottleneck in the conductivity of the overall top electrode. Furthermore, the sole ammonium sulfide passivation might not be sufficient to completely eliminate the surface states in the GaAs NWs and a SiN_x shell as additional passivation could lead to higher efficiency. Also, the junction doping levels are estimated by means of planar growth tests; however dopant incorporation could be fairly different for the crystallographic directions involved in the NW. Figure 4.3c shows a comparison in terms of *EQE* measurements between ITO and AZO. This figure of merit quantifies the ratio of the number of charge carriers output by the array solar cell to the number of photons present in the AM1.5G flux on the device.

Contact type	ITO	AZO
Trasmittance (%) **(500 nm<λ<1000 nm)**	>85	>85
Sheet R (Ω/sq)	15	627
Doping concn (cm^{-3})	8.8×10^{20}	4.8×10^{19}
Mobility (cm^2/Vs)	27	9
Measured type	N	P

Table 4.1. Optoelectrical characteristics of ITO and AZO

Although the shapes and trends are comparable over the spectrum of interest, the EQE measurement for the GaAs nanostructured solar cell processed with ITO as top electrode exhibits

a more-than-doubled carrier collection in comparison with the AZO contact. Considering fairly similar work functions, the main cause for this unexpected behavior has to be sought in the difference of electrical and optical properties of the two conducting oxides. Table 4.1 presents a comparison of the electro-optical properties of both ITO and AZO thin films on quartz substrate. The sputtering conditions are maintained exactly equal to the ones used for the top electrode depositions on the devices and carried out on quartz in order to investigate only the thin film properties. The optical transmittance is obtained through Fourier transform infrared (FTIR) spectroscopy and calibrated with a bare quartz substrate as a baseline. The magnitudes of the transmittance are analogous, above 85% in the working optical range of the solar cells. This is in accordance with similar optical refractive indices as well as extinction coefficients for both transparent oxides.

The electrical analysis of the semiconducting oxides is characterized by means of four-point probe and Hall measurements. The sheet resistance for AZO is 627 Ω/sq with a measured thickness of 680 nm whereas the sheet resistance for ITO amounts to 15 Ω/sq, for 630 nm thickness. This is in agreement with the trend observed in the J-V device characteristics under dark (Fig. 4.3a-b): the NP array processed with ITO exhibits a current of 107 μA at 2 V while the devices with AZO sputtered as top electrode show a current of 38 μA at 2 V. The Hall measurements are taken in a Van-der-Pauw geometry at room temperature under a nominal magnetic field of 2.5 T. The doping concentration and carrier mobility for the deposited ITO amount to 8.8×10^{20} cm^{-3} and 27 cm^2/Vs, respectively, with an n-type doping polarity. The same measurements for AZO reveal a doping concentration of 4.8×10^{19} cm^{-3} and a carrier mobility of

9 cm^2/Vs. The measured doping is p-type, in agreement with the presence of nitrogen during the sputtering process.[16]

Consequently, ITO performs as a transparent anodic electrode whereas AZO functions as a transparent cathodic contact. Considering one single NP as an elemental part of the device, the p-doped GaAs core is surrounded by the n-doped GaAs shell, constituting the photovoltaic junction. Under illumination, photogenerated minority carriers drift to their respective electrodes: electrons will travel along the n-doped shell whereas holes will be funneled into the p-doped core all the way to the substrate. Focusing on the top contacts, electrons will encounter a doping alignment of the type n/n^+ for n-doped shell/ITO while in the case of AZO electrons will go through an n/p^+ interface. For this reason, the extraction of the photogenerated carriers is greatly fostered when ITO is exploited as top electrode, translating into higher *PCE*s.

Finally, to verify that each NP is acting as a solar cell, high-resolution scanning photocurrent microcopy (SPCM) is used to image the array of NPs. SPCM is performed using diffractionlimited optics and a green HeNe laser (λ = 544 nm). Zero-bias photoconductivity is measured using a data acquisition board and preamplifier as the sample is scanned on a translational stage with 50 nm/step resolution in X and Y axes. The spot size of the beam is ~300 nm as determined from full-width at $1/e^2$. The laser intensity for the measurements is attenuated to 103 $\mu W/\mu m^2$ to utilize the more sensitive settings of the preamplifier given the critical pitch of the NPs and the levels of photocurrent generated by the NP arrays.

Figure 4.4a shows the SPCM map obtained for the best ITO device, with Fig. 4.4b a line scan through the image. The map clearly shows alternating regions of higher and lower photocurrent forming a square array, with spacing of 600 nm between maxima. Note that

because of the laser spot size and the close spacing between NWs, there is a nonzero photocurrent even when the laser beam is centered exactly between four NPs. The technique is able to resolve features smaller than the spot size[17] as the beam profile as well as location is of importance in generating the signal used in the microscopy.

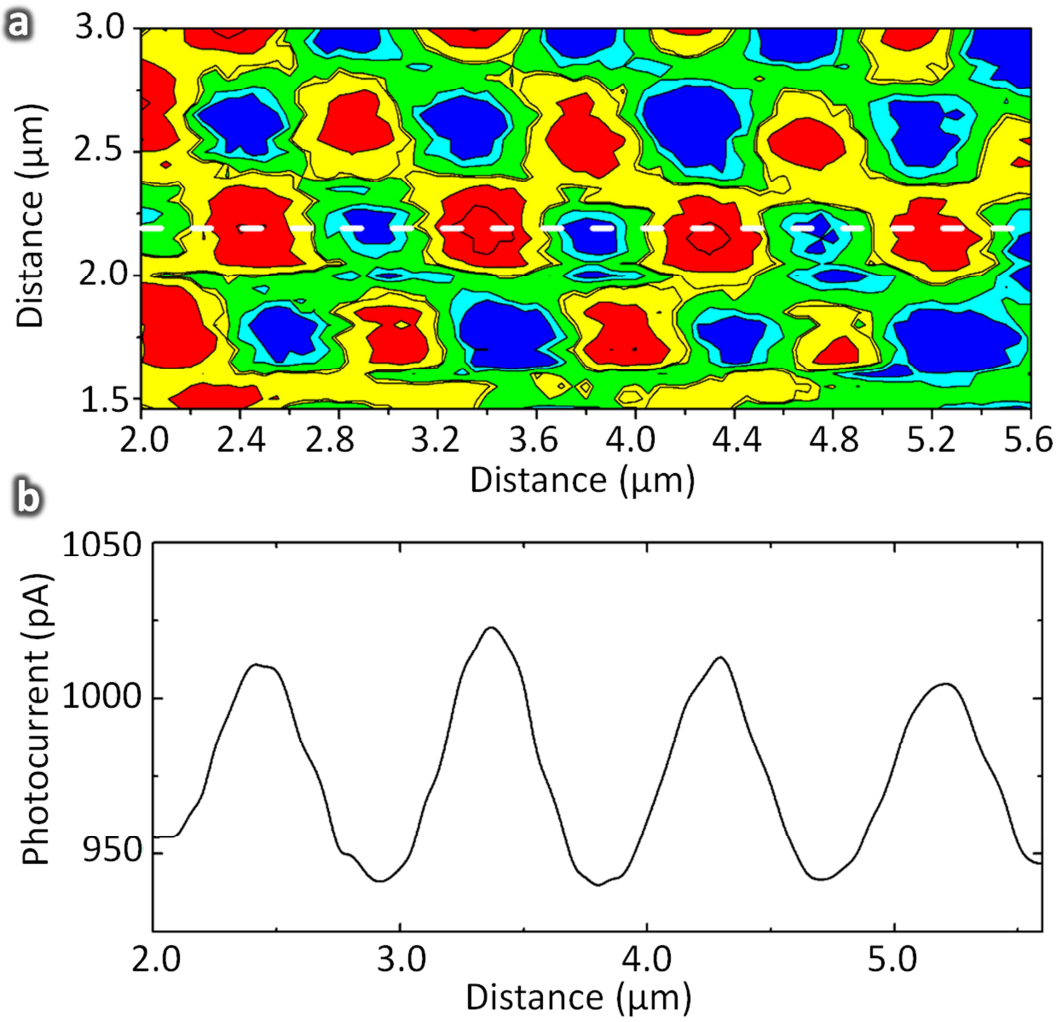

Figure 4.4. (a) Scanning photocurrent microscopy (SPCM) image of the best device processed with ITO as top transparent electrode. Red indicates largest photocurrent and blue the lowest. (b) Corresponding photocurrent line profile across the dashed line in panel a.

The current work is possibly the highest resolution display of the technique insofar as resolving dense features of known proximity. The SPCM mapping validates the fact that the collective *J-V* characteristics of the array under light are indeed the superposition of all the photocurrent contributions coming from each individual NP. Furthermore, from the laser intensity and maximum generated photocurrent, an *EQE* of 2.8% is calculated. The small discrepancy between this number and the one obtained from the full illumination of the devices is mainly attributable to the fact that the laser light is fundamentally different from a monochromatically filtered source in regards to its relative full width at half maximum.

In conclusion, this chapter presents the realization of a solar cell using a dense, uniform array of vertical core/shell NPs. Electrical characterization shows a device behavior affected by the doping type of the chosen transparent contact. *EQE* measurements quantify the difference in carrier extraction between AZO and ITO when used as top electrodes in GaAs NP photovoltaics. High-resolution SPCM characterization validates the independent functioning of each NP in the array with an individual peak photocurrent of ~1 nA at 544 nm. Device efficiencies as large as 2.54% are obtained using ITO as the transparent conducting electrode. The absence of metal catalyst during growth translates into low-leakage-current devices. These results open a route to much higher efficiencies through the improvement of architecture as well as material and interface properties.

4.4 References

1. Zhu, J., Hsu, C., Yu, Z., Fan, Z., Cui, Y. Nanodome solar cells with efficient light management and self-cleaning, *Nano Lett.* **10**, 1979-1984 (2010).

2. Zhu, J., Yu, Z., Burkhard, G. F., Hsu, C., Connor, S. T., Xu, Y., Wang, Q., McGehee, M., Fan, S., Cui, Y. Optical absorption enhancement in amorphous silicon nanowire and nanocone arrays, *Nano Lett.* **9**, 279-282 (2009).

3. Stupca, M., Alsalhi, M., Al Saud, T., Almuhanna, A., Nayfeh, M. H. Enhancement of polycrystalline silicon solar cells using ultrathin films of silicon nanoparticle, *Appl. Phys. Lett.* **91**, 063107 (2007).

4. Fan, Z., Razavi, H., Do, J., Moriwaki, A., Ergen, O., Chueh, Y., Leu, P., Ho, J., Takahashi, T., Reichertz, L., Neale, S., Yu, K., Wu, M., Ager, J., Javey, A. Three-dimensional nanopillar-array photovoltaics on low-cost and flexible substrates, *Nat. Mater.* **8**, 648-653 (2009).

5. Goto, H., Nosaki, K., Tomioka, K., Hara, S., Hiruma, K., Motohisa, J., Fukui, T. Growth of core-shell InP nanowires for photovoltaic application by selective-area metalorganic vapor phase epitaxy, *Appl. Phys. Express* **2**, 035004 (2009).

6. Huang, J.; Chiam, S.; Tan, H.; Wang, S.; Chim, W. Fabrication of silicon nanowires with precise diameter control using metal nanodot arrays as a hard mask blocking material in chemical etching, *Chem. Mater.* **22**, 4111–4116 (2010).

7. Putnam, M., Boettcher, S., Kelzenberg, M., Turner-Evans, D., Spurgeon, J., Warren, E., Briggs, R., Lewis, N., Atwater, H. Si microwire-array solar cells, *Energy Environ. Sci.* **3**, 1037-1041 (2010).

8. Green, M., Emery, K., Hishikawa, Y., Warta, W., Dunlop, E.D. Solar cell efficiency table (version 42), *Prog. Photovolt: Res. Appl.* **21**, 827-837 (2013).

9. Czaban, J. A., Thompson, D. A., LaPierre, R. R. GaAs core-shell nanowires for photovoltaic applications, *Nano Lett.* **9**, 148-154 (2009).

10. Jackson, J. B., Kapoor, D., Jun, S., Miller, M. S. J. Integrated silicon nanowire diodes and the effects of gold doping from the growth catalyst, *Appl. Phys.* **102**, 054310 (2007).

11. Lin, C., Povinelli, M. L. Optical absorption enhancement in silicon nanowire arrays with a large lattice constant for photovoltaic applications, *Opt. Express* **17**, 19371–19381 (2009).

12. Cheng, C., Chien, C., Luo, G., Chang, C., Kei, C., Yang, C., Hsiao, C., Perng, T., Chang, C. J. Electrical and material characterization of atomic-layer-deposited Al_2O_3 gate dielectric on ammonium sulfide treated GaAs substrates, *Phys.: Conf. Ser.* **100**, 042002 (2008).

13. Wakeham, S., Thwaites, M., Holton, B., Tsakonas, C., Cranton, W., Koutsogeorgis, D., Ranson, R. Low temperature remote plasma sputtering of indium tin oxide for flexible display applications, *Thin Solid Films* **518**, 1355-1358 (2009).

14. Sul, W. S., Han, H. J., Lee, H. S., Lee, B. H., Kim, S. D., Rhee, J. K. *Mater. Res. Soc. Symp. Proc.* **734**, 231-236 (2003).

15. Chiu, H.; Yang, S. Enhanced power performance of enhancement-mode $Al_{0.5}Ga_{0.5}As/In_{0.15}Ga_{0.85}As$ pHEMTs using a low-k BCB passivation, *IEEE Electron Device Lett.* **23**, 243-245 (2002).

16. Lu, H., Lu, J., Lai, C., Wu, G. Fabrication of low-resistive p-type Al-N co-doped zinc oxide thin films by RF reactive magnetron sputtering, *Phys. B* **404**, 4846-4849 (2009).

17. Ahn, Y. H., Tsen, A. W., Kim, B., Park, Y. W., Park, J. Photocurrent imaging of p-n junctions in ambipolar carbon nanotube transistors, *Nano Lett.* **7**, 3320-3323 (2007).

Chapter 5

Radial GaAs nanopillar solar cells employing in situ surface passivation

5.1 Overview

Nanometer-scaled materials[1-15] are attractive candidates to implement efficient designs for the conversion of solar energy to electricity. Colloidal quantum dots[16,17] , nanoparticles[18,19] , nanodomes[20] and nanowires[1-12,21-23] are actively investigated to improve the charge collection process along with broadband-enhanced light absorption[24] resulting from their optical trapping properties. The adoption of such materials is ultimately aimed to reduce the cost while improving the total *PCE* of the final device. In core-shell p-n junctions embedded within NPs, the electron-hole pair separation occurs in the radial direction and the photogenerated carriers have to travel distances much shorter than the minority carrier diffusion length.[23,25]

Considering that the photo-active region is represented by the nanostructures themselves, the NP arrays can be embedded in a flexible and transparent polymer (for example, polydimethylsiloxane) and peeled off from the growth substrate, which can be re-used in subsequent growth runs,[26] lowering fixed costs in manufacturing productions. III-V direct-bandgap compound semiconductors offer the chance to efficiently absorb most of the incoming photons within a couple of microns of material thickness and they enable multi-junction integration for a complete ultraviolet/visible/infrared spectral utilization.

The high surface-to-volume ratio represented by the adoption of a cylindrical radial junction increases both the active depletion region as well as the overall surface area of the device, which then becomes more susceptible to recombination of photogenerated charge carriers. Because of the surface-state charges arising from surface scattering, charge recombination and Fermi level pinning, the charge-carrying volume in the NP is much narrower compared with its physical volume, confining the carriers to a smaller conducting core.[27] The high surface recombination velocity results in the annihilation of minority carriers, which would otherwise contribute to a portion of the output in the PV device. Recent reports on ensemble of core-shell GaAs NWs applied to solar cells have revealed conversion efficiencies ranging from 0.83%[5] for as-grown devices to 2.54%[6] for devices post-treated with ammonium sulphide agents. In situ passivating techniques are widely adopted in planar optoelectronic designs to most effectively reduce the surface state density, offering the highest stability over time. Generally, thin layers of epitaxial high-bandgap materials act as a barrier to prevent carriers from recombining at the surface.[28-30]

In situ NP passivation represents a challenging task due to the different crystallographic directions[31,32] and energetics on the NP facets, while maintaining a lattice matched growth between dissimilar materials. Hence, there has been no demonstration of integrating in situ epitaxial passivation into radial-junction NP arrays for PV application thus far. Optically, vertically aligned semiconducting wires can trap solar irradiation[11,12] more effectively with respect to planar PV designs, and periodic patterns of dielectric spheres and metal particles[13] have shown to increase the probability of photon absorption. Theoretical calculations of periodic arrays of silicon wires[33] reveal a light absorption strongly tunable with respect to the geometric

properties of the nanostructures (for example, orientation, diameter, height, filling ratio). Therefore, the adoption of a growth mask on which the various geometric parameters can be determined a priori represents a solution for a controlled NP positioning.

This chapter experimentally demonstrates in situ epitaxial surface passivation of direct-bandgap GaAs NP solar cells via patterned, catalyst-free, SAE[6,34]. High-bandgap InGaP shells are grown in situ and lattice-matched on the GaAs NPs to prevent from high surface recombination rates and Fermi level pinning.[30] The patterned growth mask is optimized in terms of NP pitch and tiling pattern to maximize the enhanced optical absorption of the arrays. All devices employ a novel titanium (Ti)/ ITO annealed alloy as transparent ohmic anode.

5.2 Maximized optical absorption through geometrical tuning

Before growth, full-wave finite-difference time-domain simulations (FDTD software Lumerical) are implemented to investigate/optimize the enhanced absorption with respect to the geometrical parameters available in the growth mask design, to achieve near-perfect absorption while minimizing material usage. Tiling pattern and center-to-center pitch are considered as variables in this set of simulations and the optimized topology can be fabricated by means of the SAE growth approach. A limited number of reports of optical absorption modelling are presented in literature for periodic arrays of III-V NPs. Geometrical tuning of InAs nanowires[33] is demonstrated both experimentally and theoretically for square-tiling patterns. Periodic arrays of GaAs NPs are investigated in terms of optical absorption with varying diameter over-pitch ratios,[44] in square pattern arrangements. The reports pervasively consider bare periodic arrays of

nanowires (not sufficient for a practical nanowire solar cell). Hence, it is necessary to model the optical properties of the final device.

Figure 5.1a represents the 3D schematic of the complete, fully processed simulated structure. Figure 5.1b displays the triangular, square, rectangular and parallelogram lattice geometries.

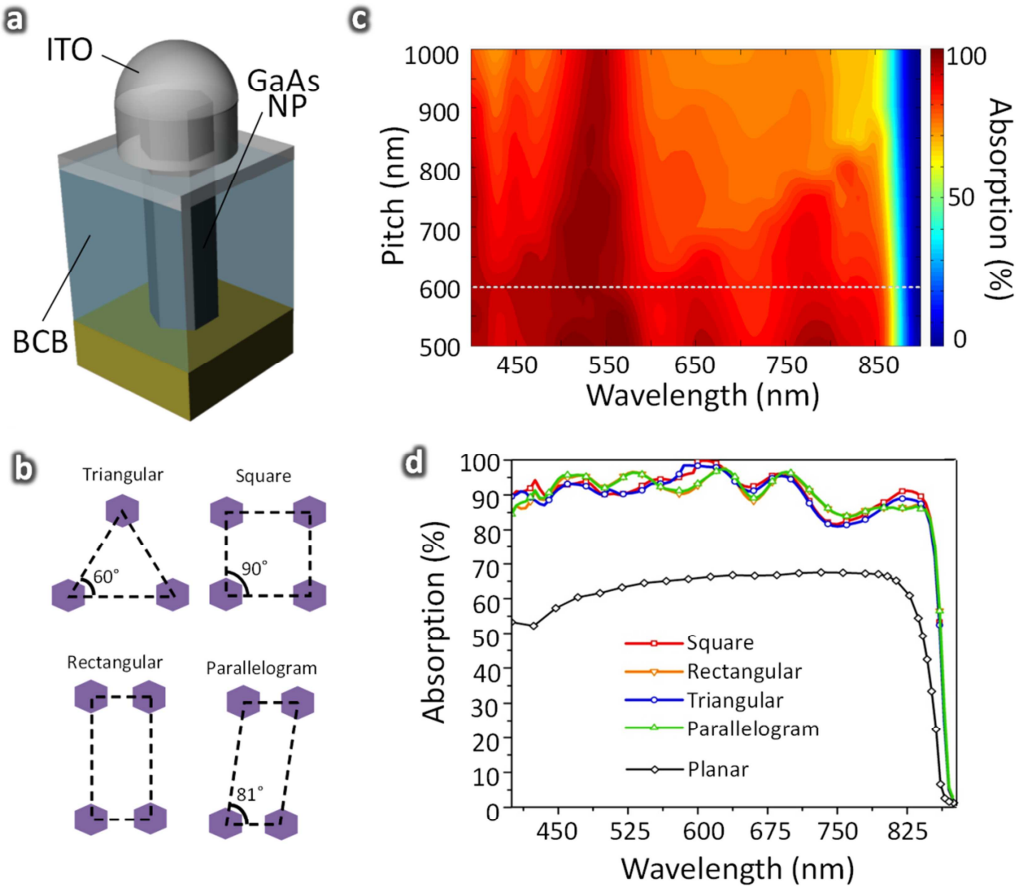

Figure 5.1. (a) 3D schematic of the complete structure used in the finite-difference time-domain simulations. To notice, the NP is embedded in the BCB layer and capped by a conformal layer of ITO as transparent top electrode. (b) Unit cells of triangular, square, rectangular and parallelogram tiling patterns are investigated. (c) 2D contour plot of NP pitch P (500 nm<P<1000 nm) and wavelength-dependent optical absorption. Red colour indicates high absorption and blue colour corresponds to low absorption. (d)Wavelength-dependent absorption as a function of different tiling patterns for a fixed 600-nm pitch (dashed cutline from Fig.5.1c).

The incident light contains both x and y polarizations to better match the unpolarized solar spectrum. Periodic boundary conditions are considering an infinite array of NPs. The NP height and diameter are fixed at 1.3 mm and 260 nm, respectively. Figure 5.1c represents a 2D contour plot of wavelength-dependent absorption (400 nm-900 nm) as a function of center-to-center pitch (500 nm-1000 nm) with a color legend spanning from low absorption (dark blue) to high absorption (dark red) values.

The plot shows that, with lower pitch size or equivalently a higher filling ratio, the absorption of the periodic structure increases. The result is expected owing to the fact that optical resonance-guided modes increase the electromagnetic light intensity, resulting from the coupling of the normally incident light to high-Q leaky modes of the periodic structure.[35] For decreasing pitch values, the light is greatly confined in the NP array and excites optical resonance-guided modes[36,37] which in turn greatly enhance the optical absorption.

Hence, a pitch size of 600 nm is chosen here as an optimized device dimension, also considering that radii below 100 nm can hardly accommodate quasi-neutral regions on both core and shell sides for an efficient carrier extraction at the ohmic electrodes. In Fig. 5.1d, four different tiling patterns (as shown in Fig. 5.1b) with optimized 600 nm pitch are compared with respect to GaAs planar substrates. The areas for the unit cell in all four patterns are identical (600 nm × 600 nm); as a result, the filling ratio is kept constant, and only the effect of tiling pattern is taken into account in this comparison. From the simulations, it can be concluded that tiling pattern does not substantially change the absorption spectrum compared with pitch size, or filling ratio, which is the governing factor in determining the absorption efficiency. Slight variations are attributed to the differences in the symmetry of the geometries.

This result is non-trivial in light of the fact that previous works[38] on periodic non-subwavelength silicon microwires (several microns for both pitch and diameter) exhibited varying optical properties depending on the periodic arrangement adopted.

5.3 Array growth and device engineering

The growth structure for GaAs NP solar cells is presented in Fig. 5.2a. The III-V NPs are formed by catalyst-free, selective-area MOCVD on masked n^+-doped (111)B GaAs substrates using hydrogen carrier gas at 60 Torr. The n-doped GaAs NPs are grown at 735 °C.

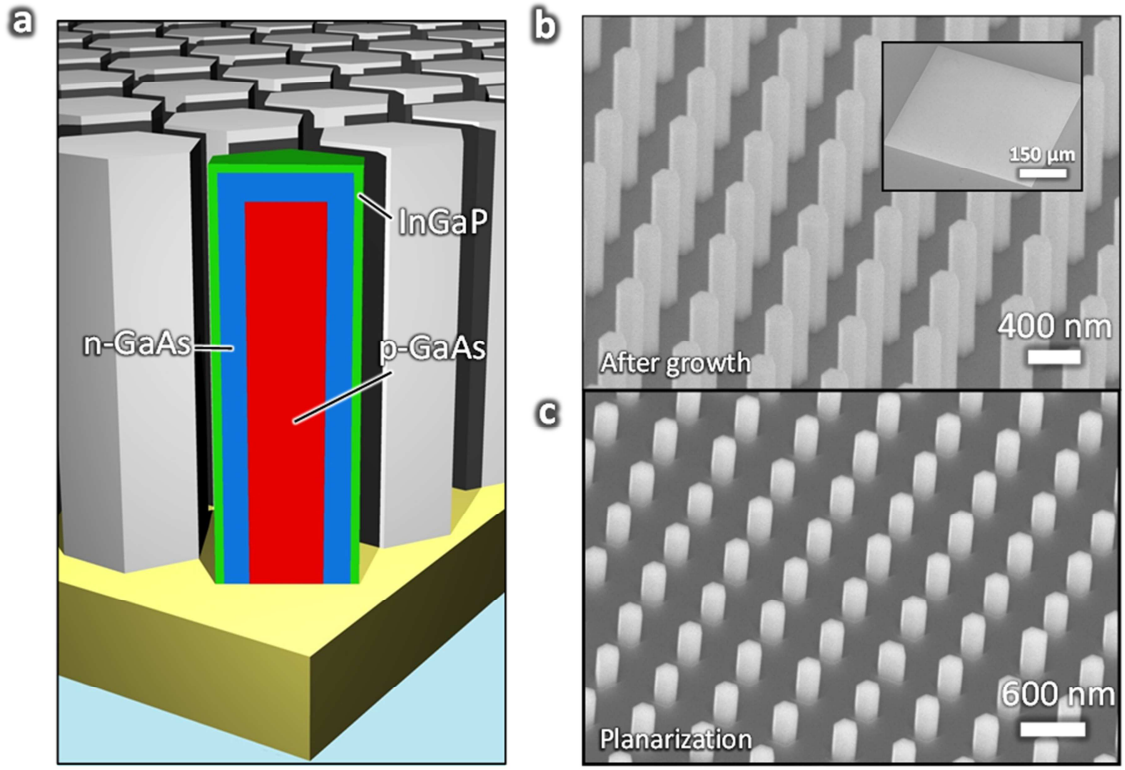

Figure 5.2. (a) Schematic drawing of the GaAs radial p–n junctions with the InGaP-passivating shell (not to scale). (b) A 45°-tilt SEM image of a typical array of GaAs NPs grown by MOCVD technique with an optimized 600 nm pitch. Scale bar, 400 nm. Inset: selective-area epitaxial approach allows to position the array and define the growth arrangement by means of a patterned dielectric mask onto the substrate. Scale bar, 150 mm. (c) A 45°-tilt SEM image of an NP array after planarization and subsequent etch-back. This step is necessary to spatially separate the anode from the cathode in the photovoltaic cells to prevent top–bottom shunting. Scale bar, 600 nm.

Subsequently, the p-doped GaAs shells and InGaP shells are both grown at 600 °C. The primary precursors used during growth are tri-methyl-gallium, tertiary-butyl-arsine, trimethyl-indium and tertiary-butyl-phosphorus. The doping sources are tetra-ethyl-tin and di-methyl-zinc as the n-type and p-type dopants, respectively, and calibrated flow rates from planar test measurements are selected to achieve carrier densities of $N_{a,core} = 1 \times 10^{17}$ cm^{-3} and $N_{d,shell} = 1 \times 10^{18}$ cm^{-3}. Once the radial p-n junction is formed, an InGaP shell lattice matched to GaAs is grown. In this fashion, an estimated GaAs core diameter of 180 nm, GaAs shell thickness of 40 nm and InGaP-passivating shell of 5 nm are formed, with a final NP height of 1.3 mm. The InGaP layer results into a negligible absorption for such thin epitaxial window. The total active area amounts to 500 µm × 500 µm and is univocally defined during the patterning process.

Figure 5.2b shows a 45°-tilted SEM image of typical in situ passivated GaAs core-shell NP arrays after epitaxy. The growth is uniform across the whole masked area as it appears from the inset. Subsequent to SAE, ohmic bottom contacts are formed by annealing a gold-germanium/nickel/gold metal alloy to the highly doped substrates. The NP arrays are then planarized with BCB that represents a transparent electrical insulator to well separate in space the top anode from the bottom cathode. After hard curing and dry etchback of the BCB, ~350 nm of the NP tips are exposed and ready to be contacted as displayed in Fig. 5.2c. BCB represents a suitable planarizing polymer with optical transparency in excess of 99%.

5.3.1 Transparent ohmic contact as an efficient hole collector

The ITO/GaAs interface has been reported in several works to be either ohmic[39] or Schottky[40,41] depending on deposition conditions and post-deposition treatments. Although characterized by n-polarity, ITO films can result into either Schottky or ohmic contacts to both n- and p-GaAs. To achieve an ohmic interface, high annealing temperatures are necessary (550-700 °C). This could detriment the epitaxial NP crystal grown at comparable temperatures.

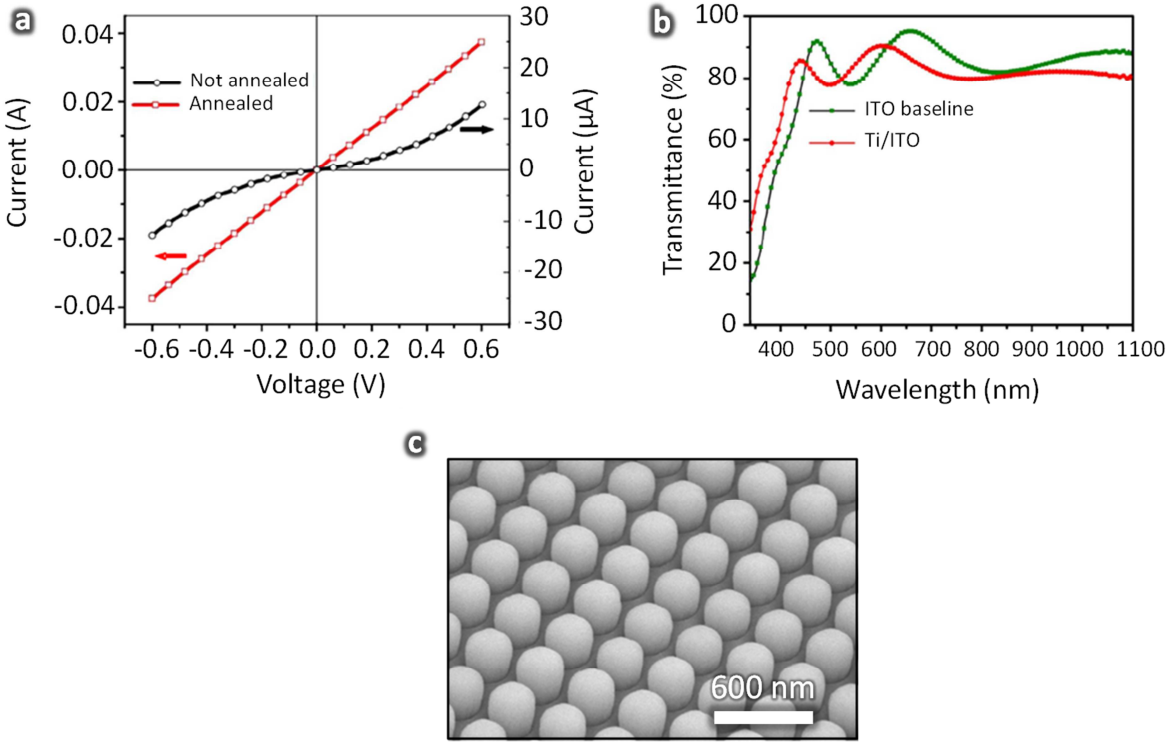

Figure 5.3. (a) *I-V* measurements of sputtered Ti/ITO alloy on p-type GaAs exhibiting a clear back-to-back Schottky characteristic before thermal annealing (black circles). Subsequent to a 300 °C treatment, an ohmic behaviour is observed with high conduction currents across the transparent contact/semiconductor interface (red squares). (b) Fourier transform infrared spectroscopy measurements of optical transmittance for a standard indium tin oxide baseline compared with a Ti/ITO film (both on quartz slides). A thin titanium interlayer (~4 nm) still ensures an acceptable optical transparency over the spectral regime of interest. (c) SEM image of sputtering deposition which exhibits a uniform, wrap-around contact morphology at the NP tips. Scale bar, 600 nm.

Conversely, rectifying contacts resulting from parasitic Schottky barriers can create wide depletion regions, forcing the carriers to overcome the potential barrier by thermionic emission.[42] Despite fundamental, these transport properties at the electrode interface have been so far overlooked, and only a few theoretical reports discuss these effects in GaAs nanowire-based solar cells.[43] With metals, Ti/Au ohmic contacts to p-GaAs are routinely achieved with very low resistance,[44] without requiring any thermal annealing step. For this reason, Ti (4 nm)/ ITO (350 nm) thin films are RF sputtered and calibrated on p-GaAs substrates ($N_{sub} \sim 10^{18}$ cm^{-3}) at room temperature in one single run to prevent oxidation of the Ti layer. Plasma-assisted sputtering is chosen here as it forms a 3D wrap-around contact to ensure a uniform carrier extraction.

The deposition is divided into two major segments. First, a continuous metallic Ti thin film is deposited at low deposition rates (~1 nm/min). Second, a 350-nm ITO overlayer is sputtered. Subsequently, *I-V* measurements are carried out to assess the transport properties of the multi-layered electrode. Figure 5.3a plots out the *I-V* characteristics. The as-sputtered Ti/ITO film exhibits a clear Schottky behaviour, with conduction currents in the microampere range. After low-temperature (300 °C) thermal annealing, the contact shows remarkable ohmic properties, with current values in fractions of ampere range. Figure 5.3b shows Fourier transform infrared spectroscopy measurements (from 340 nm-1100nm wavelength) of optical transmittance for a standard ITO baseline compared with a Ti/ITO film (both on quartz slides). Despite a small transmittance drop, the optimized electrode is highly transparent and therefore can be utilized to contact the p-GaAs shells in the NP arrays. Following a selective chemical wet etch of the InGaP shells at the NP tips (Fig. 5.2c), the Ti/ITO alloy is conformally deposited as top anode as shown in Fig. 5.3c and thermally annealed with a four-probe-measured sheet resistance of 12.5 Ω/sq.

5.4 Results and discussion

Figure 5.4a displays the *J-V* characteristic under dark of a typical, fully processed, GaAs core-shell NP solar cell with InGaP-passivating shell. The data is plotted in semi-log axis to correctly extrapolate reverse bias leakage current, rectification ratio, ideality factor and series resistance values. Low leakage currents in the order of ~30 nA at -1 V are consistently measured. Rectification ratios of up to ~10^5 (@ ± 1V) are achieved. A fitting curve in the diffusion current region reveals ideality factors of n ~ 1.58. These values can be attributed to several factors.

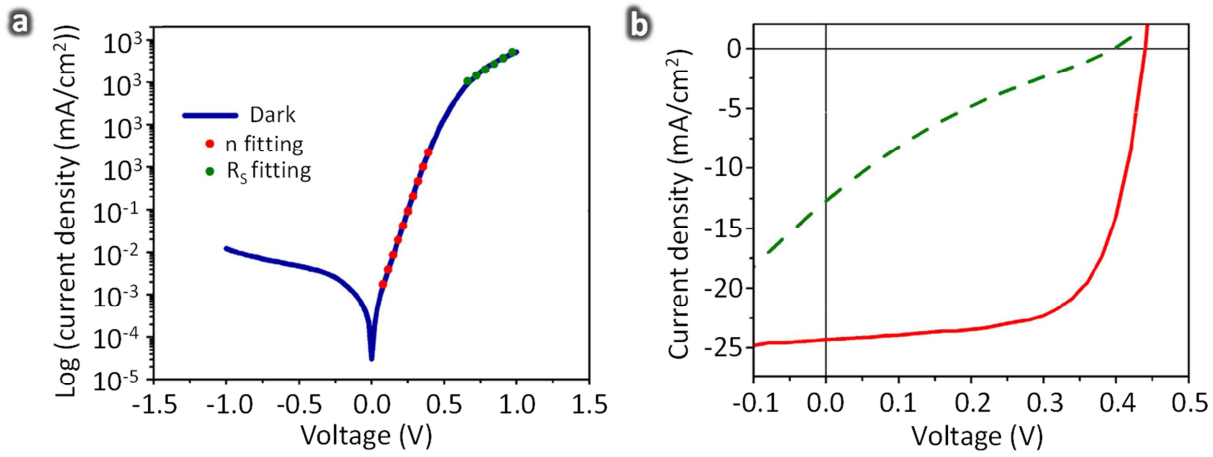

Figure 5.4. (a) Semi-log dark current-voltage characteristic of a typical GaAs NP array. Both ideality factors (n ~ 1.58, red dots) and high-injection series resistance (Rs ~530 Ω, green dots) are extrapolated by means of fitting curves. The type of carrier transport is well below the space-charge-limited model (n>2). The good diodic behavior is corroborated by a $10^{4.7}$ rectification ratio. (b) Current density-voltage characteristics under air mass 1.5 global illumination conditions for photovoltaic devices with (solid red line) and without in situ InGaP shell (dashed green line). InGaP-passivated photovoltaic cells show an open-circuit voltage of 0.44 V, short-circuit current density of 24.3 mA/cm^2 and FFs of 62%. This translates into a *PCE* that amounts to 6.63%.

5.4.1 Enhanced efficiency using InGaP passivation

First, the SAE approach does not require any catalyst[34] (e.g. gold or copper) to initiate the growth, avoiding any metal incorporation within the GaAs crystal that has been reported to increase the reverse bias leakage current in nanowire-based devices.[45] Second, the high-bandgap InGaP shell minimizes the surface state density on the nanofacets that could partly deplete the inner n-p core-shell junction. This is witnessed by the fact that the ideality factor is far below the space-charge-limited condition ($n > 2$). In high-injection regime, a series resistance $Rs \sim 530\ \Omega$ is extrapolated from the fitting curve $R_S = V/I$. The NP-based solar cells are then tested under AM1.5G illumination conditions (calibrated 1 sun), at room temperature.

Figure 5.4b illustrates *J-V* characteristics under light for devices with and without in situ epitaxial passivation. For PV devices without InGaP shells (dashed line), V_{OC} of 0.37 V and J_{SC} of 12.8 mA/cm^2 with *FF* of 21% are observed. This translates into *PCE* of up to 1.02%. The 'S-shape' kink in the *J-V* characteristic is indicative of interfacial effects such as surface dipoles, defects and traps that create barriers for carrier extraction.[46] This effect leads to a loss in both J_{SC} and *FF*, evidently reducing the *PCE* of the final device. In case of core–shell junctions capped with InGaP shells, the optoelectronic properties are markedly improved: V_{OC} = 0.44 V, J_{SC} = 24.3 mA/cm^2 and *FF* = 62 %. This results into a final *PCE* of 6.63%. InGaP is reducing surface states as confirmed by high FF and J_{SC}. The V_{OC} value is increased by ~20% compared with un-passivated devices and it is the highest measured in GaAs NP-array PVs.

V_{OC} values of ~0.9 V are expected for planar GaAs solar cells.[47] This discrepancy can be attributed to the fact that the surface state density is being effectively alleviated but not suppressed altogether. From measurements on single GaAs NP-field effect transistors, the

surface state densities before and after InGaP surface passivation decreases from 5×10^{12} cm^{-2} eV^{-1} to 7×10^{10} $cm^{-2}eV^{-1}$, respectively.[48] Furthermore, the measured V_{OC} is a collective figure of merit resulting from ~2.8×10^{8} p-n junctions per cm^2 (considering a square-lattice arrangement, 600 nm pitch) connected in parallel. For this reason, dopant incorporation inhomogeneities and/or defective NPs within the whole array can severely lower the final V_{OC} at the terminals. The NPs constituting the whole array are required to be almost electrically and optically identical. Recent studies on dopant mapping in NPs, showed doping variations in excess of two orders of magnitude along both axial and radial directions,[49-51] raising clear differences with respect to a canonical abrupt, metallurgical planar p–n junction.

5.4.2 Enhanced EQE using InGaP passivation

Figure 5 *EQE* curves for devices with and without passivation. The measurements are taken from 340-1000 nm.

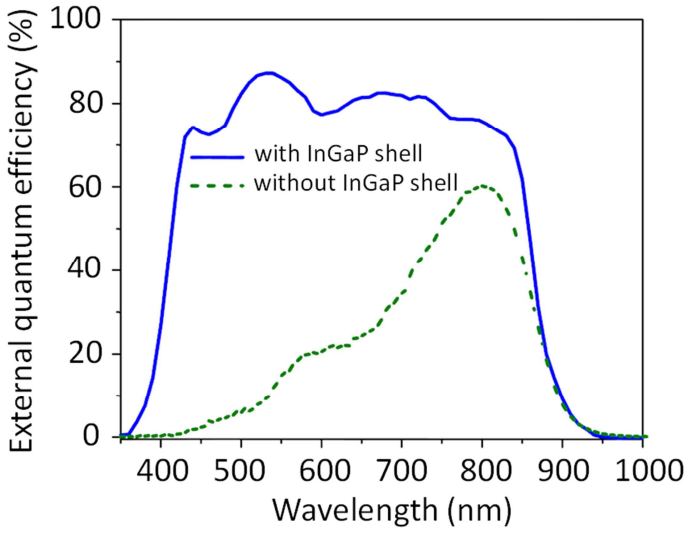

Figure 5.5. *EQE* measurements of processed GaAs NP solar cell devices with (solid blue line) and without (dashed green line) wide-bandgap in situ passivation.

The *EQE* values for the NP arrays capped with InGaP shells are well above 70% in the spectral regime of interest (blue solid line), with a peak efficiency of ~86% at 520 nm. For bare-grown radial p-n junctions, high energy photons are possibly recombining at the surface (green dashed line). This is due to the fact that high-energy photons have shorter penetration depths into GaAs compared to infrared photons, therefore being the most sensitive to recombination centers at the surface.[52] Consequently, the *EQE* response is considerably reduced especially in the ultraviolet-visible spectral region when in situ passivation is not adopted.

Device structure	Growth method	Contact scheme	Passivation method	V_{OC} (V)	J_{SC} (mA/cm^2)	FF (%)	PCE (%)
n-p (axial)[53]	MBE	Local probing	None	0.24	27.3	25	1.65
p-n (radial)[6]	MOCVD	ITO or AZO	Acqueous ammonium sulfide	0.39	17.6	37	2.54
p-n (radial)[5]	MBE	ITO	None	0.2	15.5	27	0.83
n-p (radial) (this work)	MOCVD	Ohmic Ti/ITO	InGaP shells	0.44	24.3	62	6.63

Table 5.1 Comparative performance of GaAs nanowire-array photovoltaics.

Table 5.1 summarizes the most recent results on arras of GaAs NPs employed in PV devices.[5,6,53] Particular emphasis is dedicated to different contact schemes and passivation techniques employed. To notice it is the dramatic *PCE* improvement once a high bandgap passivation technique is introduced. Also, a tested ohmic contact at the transparent electrode/semiconductor interface leads to considerably higher FF values.

This chapter reports the highest efficiency to date for GaAs-based NP-array solar cells employing InGaP in situ passivation with an overall *PCE* of 6.63% under AM1.5G conditions. Thermally annealed Ti/ITO ohmic contacts ensure a good carrier extraction at the top anode while preserving an overall transparency/optical coupling with the NP arrays. Photoelectrical

measurements highlight the necessity of an in situ passivation treatment to dramatically improve *EQE* (above 70%) as well as the total *PCE*. The array architecture offers a path for a practical large area scaled-up solar cell, in opposition with the pervasive characterization of single-NP PVs. These results lay the ground to considerably higher efficiencies in III-V NP-based photovoltaics and open up a route for NP-based multi-junction architectures by means of a careful investigation of contact interface, surface state density and epitaxial growth of dissimilar materials.

5.5 References

1. Willardson, R., Beer, A. Optical properties of III-V compounds Vol. **3**, *Academic Press* (1967).

2. Shur, M. Physics of semiconductor devices, *Prentice Hall* (1990).

3. Wu, P., Anttu, N., Ku, H., Samuelson, L., Pistol, M.-E. Colorful InAs nanowire arrays: from strong to weak absorption with geometrical tuning, *Nano Lett.* **12**, 1990-1995 (2012).

4. Wen, L., Zhao, Z., Li, X., Shen, Y., Guo, H., Wang, Y. Theoretical analysis and modeling of light trapping in high efficicency GaAs nanowire array solar cells, *Appl. Phys. Lett*. **99**, 143116 (2011).

5. Czaban, J., Thompson, D., LaPierre, R. GaAs core-shell nanowires for photovoltaic applications, *Nano Lett.* **9**, 148-154 (2009).

6. Mariani, G., Wong, P.-S., Katzenmeyer, A.M., Leonard, F., Shapiro, J., Huffaker, D.L. Patterned radial GaAs nanopillar solar cells, *Nano Lett*. **11**, 2490-2494 (2011).

7. Goto, H., Nosaki, K., Tomioka, K., Hara, S., Hiruma, K., Motohisa, J., Fukui, T. Growth of core-shell InP nanowires for photovoltaic application by selective-area metalorganic vapor phase epitaxy, *Appl. Phys. Express* **2**, 035004 (2009).

8. Wei, W., Bao, X.Y., Soci, C., Ding, Y, Wang, Z.L., Wang. D. Direct heteroepitaxy of vertical InAs nanowires on Si substrates for broad band photovoltaics and photodetection, *Nano Lett.* **9**, 2926-2934 (2009).

9. Tomioka, K., Tanaka, Tomotaka, Hara, S., Hiruma, K., Fukui, T. III-V nanowires on Si substrate: selective-area growth and device application, *IEEE J. Sel. Top. Quant. Electron.* **17**, 1112-1129 (2011).

10. Takahashi, T., Takei, K., Adabi, E., Fan, Z., Niknejad, A., Javey, A. Parallel array InAs nanowire transistors for mechanically bendable, ultrahigh frequency electronics, *ACS Nano* **4**, 5855-5860 (2010).

11. Kupec, J., Stoop, R., Witzigmann, B. Light absorption and emission in nanowire array solar cells, *Opt. Express* **18**, 27589-27605 (2010).

12. Anttu, N., Xu, H. Q. Coupling of light into nanowire arrays and subsequent absorption, *J. Nanosci. Nanotechnol.* **10**, 7183-7187 (2010).

13. Polman, A., Atwater, H. Photonic design principles for ultrahigh-efficiency photovoltaics, *Nat. Mater.* **11**, 174-177 (2012).

14. Yu, Z., Raman, A., Fan, S. Fundamental limit of nanophotonic light trapping in solar cells, *PNAS* **41**, 17491-17496 (2010).

15. Kamat, P. Meeting the clean energy demand: nanostructure architectures for solar energy conversion, *J. Phys. Chem. C* **7**, 2834-2860 (2007).

16. Pattantyus-Abraham, A.G., Kramer, I.J., Barkhouse, A.R., Wang, X., Kostantanos, G., Debnath, R., Levina, L., Raabe, I., Nazeeruddin, M.K., Gratzel, M., Sargent, E.H. Depleted-heterojunction colloidal quantum dot solar cells, *ACS Nano* **6**, 3374-3380 (2010).

17. Zhaon N., Osedach, T.P., Chang, L.Y., Geyer, S.M., Wanger, D., Binda, M.T., Arango, A.C., Bawendi, M.G., Bulovic, V. Colloidal PbS quantum dot solar cells with high fill factor, *ACS Nano* **7**, 3743-3752 (2010).

18. Derkacs D., Lim S., Matheu P., Mar W., Yu E. Improved performance of amorphous silicon solar cells via scattering from surface plasmon polaritons in nearby metallic nanoparticles, *Appl. Phys. Lett.* **89**, 093103 (2006).

19. Yao, Y., Yao, J., Narashimhan, V.K., Ruan, Z., Xie, C., Fan, S., Cui. Y. Broadband light management using low-Q whispering gallery modes in spherical nanoshells, *Nat. Commun.* **3**, 664 (2012).

20. Zhu J., Hsu C., Yu Z., Fan Z. & Cui Y. Nanodome solar cells with efficient light management and self-cleaning, *Nano Lett.* **10**, 1979-1984 (2010).

21. Putnam, M., Boettcher, S., Kelzenberg, M., Turner-Evans, D., Spurgeon, J., Warren, E., Briggs, R., Lewis, N., Atwater, H. Si microwire-array solar cells, *Energy Environ. Sci.* **3**, 1037-1041 (2010).

22. Garnett E., Yang P. Silicon nanowire radial p-n junction solar cells, *JACS* **28**, 9224-9225 (2008).

23. Tang J., Huo Z., Brittman S., Gao H. & Yang P. Solution-processed core-shell nanowires for efficient photovoltaic cells, *Nat. Nanotechnol.* **6**, 568-572 (2011).

24. Agrawal M. & Peumans P. Broadband optical absorption enhancement through coherent light trapping in thin-film photovoltaic cells, *Opt. Express* **8**, 5385-5396 (2008).

25. Tian, B., Zheng, X., Kempa, T.J., Fang, Y., Yu, N., Yu, G., Huang, J., Lieber, C.M. Coaxial silicon nanowires as solar cells and nanoelectronic power sources, *Nature* **449**, 885-889 (2007).

26. Spurgeon, J.M., Plass, K.E., Kayes, B.M., Brunschwig, B.S., Atwater, H.A., Lewis, N.S. Repeated epitaxial growth and transfer of arrays of patterned, vertically aligned, crystalline Si wires from a single Si(111) substrate, *Appl. Phys. Lett.* **93**, 032112 (2008).

27. Bjork M., Schmid H., Knoch J., Riel H., Riess W. Donor deactivation in silicon nanostructures. *Nat. Nanotechnol.* **4**, 103-107 (2009).

28. Knorr K., Pristovsek M., Resch-Esser U., Esser N., Zorn M., Richter W. In-situ surface passivation of III-V-semiconductors in MOVPE by amorphous As and P layers, *J. Cryst. Growth* **170**, 230-236 (1997).

29. Algora del Valle, C., Alcazar, M. Performance of antireflecting coating-AlGaAs window layer coupling for terrestrial concentrator GaAs solar cells, *IEEE Trans. Elec. Dev.* **9**, 1499-1506 (1997).

30. Pla, J., Barrera, M., Rubinelli, F. The influence of the InGaP window of GaAs solar cells, *Semicond. Sci. Technol.* **22**, 1122-1130 (2007).

31. Dan, Y., Seo, K., Takei, K., Meza, J.H., Javey, A., Crozier, K.B. Dramatic reduction of surface recombination by in situ surfacepassivation of silicon nanowires, *Nano Lett.* **11**, 2527-2532 (2011).

32. Hu, S., Kawamura, Y., Huang, K.C.Y., Li, Y., Marshall, A.F., Itoh, K.M., Brongersma, M.L., McIntyre, P.C. Thermal stability and surface passivation of Ge nanowires coated by epitaxial SiGe shells, *Nano Lett.* **12**, 1385-1391 (2012).

33. Alaeian, H., Atre, A., Dionne, J. Optimized light absorption in Si wire array solar cells, *J. Opt.* **14**, 024006 (2012).

34. Shapiro, J. N., Lin, A., Wong, P. S., Scofield, A. C., Tu, C., Senanayake, P. N., Mariani, G., Liang, B. L., Huffaker, D. L. InGaAs heterostructure formation in catalyst-free GaAs nanopillars by selective-area metal organic vapor phase epitaxy, *Appl. Phys. Lett*. **97**, 243102 (2010).

35. Cao, L., White, J.S., Park, J.S., Schuller, J.A., Clemens, B.M., Brongersma, M.L. Engineering light absorption in semiconductor nanowire devices, *Nat. Mater*. **8**, 643-647 (2009).

36. Lin C., Povinelli M. Optical absorption enhancement in silicon nanowire arrays with a large lattice constant for photovoltaic applications, *Opt. Express* **17**, 19371–19381 (2009).

37. Yu H., Li Y. Nanoscale gold intercalated into mesoporous silica as a highly active and robust catalyst, *Nanotecnology* **23**, 294010 (2012).

38. Kelzenberg, M.D., Boettcher, S.W., Petykiewicz, J. A., Turner-Evans, D.B., Putnam, M. C., Warren, E.L., Spurgeon, J.M., Briggs, R.M., Lewis, N.S., Atwater, H.A. Enhanced absorption and carrier collection in Si wire arrays for photovoltaic applications, *Nat. Mat.* **9**, 239-244 (2010).

39. Davies D., Morgan D., Thomas H. Indium-based ohmic contacts to n-GaAs, fabricated using an ion-assisted deposition technique, *Semicond. Sci. Technol.* **14**, 615-620 (1999).

40. Balasubramanuan N., Subrahmanyam S. Schottky barrier at the indium tin oxide-n-GaAs interface: effect of surface arsenic deficiency, *Thin Solid Films* **193**, 528–535 (1990).

41. Morgan D., Aliyu Y., Bunce R. The thermal stability of indium-tin-oxide/n-GaAs schottky contacts, *Phys. Stat. Sol. A Appl. Res.* **1**, 77–93 (1992).

42. Padovani F. Thermionic emission in Au-GaAs Schottky barriers, *Solid State Electron.* **2**, 193-200 (1968).

43. Tajik N., Peng Z., Kuyanov P., LaPierre R. Sulfur passivation and contact methods for GaAs nanowire solar cells, *Nanotech.* **22**, 225402 (2011).

44. Paktar M., Chin T., Woodall J., Lundstrom M., Melloch M. Very low resistance nonalloyed ohmic contacts using low-temperature molecular beam epitaxy of GaAs, *Appl. Phys. Lett.* **66**, 1412 (1995).

45. Jackson J., Kapoor D., Jun S., Miller M. Integrated silicon nanowire diodes and the effects of gold doping from the growth catalyst, *J. Appl. Phys.* **102**, 054310 (2007).

46. Kumar A., Sista S., Yang. Y. Dipole induced anomalous S-shape I-V curves in polymer solar cells, *J. Appl. Phys.* **105**, 094512 (2009).

47. Ghandhi S., Mathur G., Rode H., Borrego J. Fabrication of p^+-n junction GaAs solar cells by a novel method, *Solid State Electron.* **12**, 1149-1152 (1984).

48. Lin, A., Shapiro, J. N., Senanayake, P. N., Scofield, A. C., Wong, P. S., Liang, B., Huffaker, D. L. Extracting transport parameters in GaAs nanopillars grown by selective-area epitaxy, *Nanotechnology* **23**, 105701 (2012).

49. Koren E., Berkovitch N., Rosenwaks Y. Measurement of active dopant distribution and diffusion in individual silicon nanowires, *Nano Lett.* **10**, 1163-1167 (2010).

50. Garnett E., Tseng Y., Khanal D., Junqiao W., Bokor J., Yang P. Dopant profiling and surface analysis of silicon nanowires using capacitance–voltage measurements, *Nat. Nanotechnol.* **4**, 311-314 (2009).

51. Perea, D.E., Hemesath, E.R., Schwalbach, E.J., Lensch-Falk, J.L., Voorjees, P.W., Lauhon, L.J. Direct measurement of dopant distribution in an individual vapour-liquid-solid nanowire, *Nat. Nanotechnol.* **4**, 315-319 (2009).

52. Kurtz, S.R., Olson, J.M., Friedman, D.J., Geisz, J.F., Bertness, K.A., Kibbler, A.E. Passivation of interfaces in high-efficiency photovoltaic devices., *MRS Spring Meet.* **573**, 95-106 (1999).

53. Cirlin, G.E., Bouravleuv, A.D., Soshnikov, I.P., Samsonenko, Y.B., Dubrovskii, V.G., Arakcheeva, E.M., Tanklevskaya, E.M., Werner, P. Photovoltaic properties of p-doped GaAs nanowire arrays grown on n-type GaAs(111)B substrate, *Nano. Res. Lett.* **5**, 360–363 (2010).

Chapter 6

Direct-bandgap core-multishell nanopillar solar cells featuring subwavelength optical concentrators

6.1 Overview

Nanopillar photonics has recently enabled advances in several research fields including optical modulators,[1] light-emitting sources,[1,2] photodetectors,[3-5] and solar cells.[6-9] Semiconductor NPs have exhibited exciting *(1)* optical properties in terms of tunability and enhanced absorption[10] and *(2)* electrical properties of radial junctions in terms of charge separation more tolerant to material defects.[11] For these reasons, a considerable body of literature is exploiting NPs as next-generation photovoltaic elements. Nanometer-sized footprint of NPs allows for a dissimilar material integration, where lattice matching requirements due to strain accommodation are relaxed. For instance, silicon NWs can be grown on a wide variety of substrates[12] and also direct-bandgap III-V NPs can be synthesized on inexpensive platforms.[13,14]

In addition, the NPs can be released from the native substrate and integrated into flexible,[15] low-cost photovoltaic devices. To analyze the interaction of a normally incident optical field with semiconducting NPs, single-NW devices are generally fabricated by dispersing the nanostructures onto an oxide-coated silicon substrate. Previous works demonstrated optical absorption engineering through leaky-mode resonances[10] arising from the subwavelength confinement of light.

Furthermore, polarization-resolved EQE spectra exhibited diameter-dependent peaks, tunable by morphological design of the structures.[7] However, the strength of NP photovoltaics manifests when arrays of 3D, vertically aligned NPs are considered collectively: light trapping increases the effective optical path length of the incoming photons, exceeding the $2n^2$ Lambertian limit under certain conditions.[16] This effect enhances considerably the absorption of solar radiation with respect to planar architectures. The adoption of a periodic, position controlled NP array can be employed to tune the corresponding absorption properties. Specific values, such as diameter (D) and pitch (P), can strongly affect the propagation of light in the subwavelength regime,[17] where the sequence of high refractive index III-V material and air can be formalized by the effective medium approximation theory.

Direct-bandgap III-V compounds benefit from extremely high optical absorption coefficients, resulting into ~100 times thinner material required to absorb 90% of above-bandgap solar photons[11] compared to silicon. Furthermore, a rigorous analysis of several III-V semiconductors including InP,[18] InAs,[19] and GaAs[17] NP arrays report wideband absorption values approaching unity. Nonetheless, photon-to-electron *PCE*s of NP-array photovoltaics based on this class of materials remain limited to 3.37%,[6] under AM1.5G. Hence, it becomes necessary to intimately correlate the optical properties of the fully integrated device structure (that will interface to the external optical field) with the electrical properties of the NP solar cell measured at the terminals.

This chapter directly correlates FDTD simulations with *J-V* and *EQE* experimental data of GaAs p-i-n core-multishell NP solar cells capped with InGaP window shells, with a measured AM1.5G *PCE* of 7.43%. The analysis highlights a residual surface state density after epitaxial

passivation and an appreciable optical focusing effect arising from dome-shaped ITO layer that intensifies and concentrates the optical field within the NP. At short wavelengths, the lenslike behavior is localized at the NP tip, whereas at longer wavelengths the light field penetrates deeper, yet confined into the nanostructure.

6.2 Device structure and photocurrent measurements

The GaAs NP solar cells consist of a core-multishell structure as shown in the schematic of Fig. 6.1a.

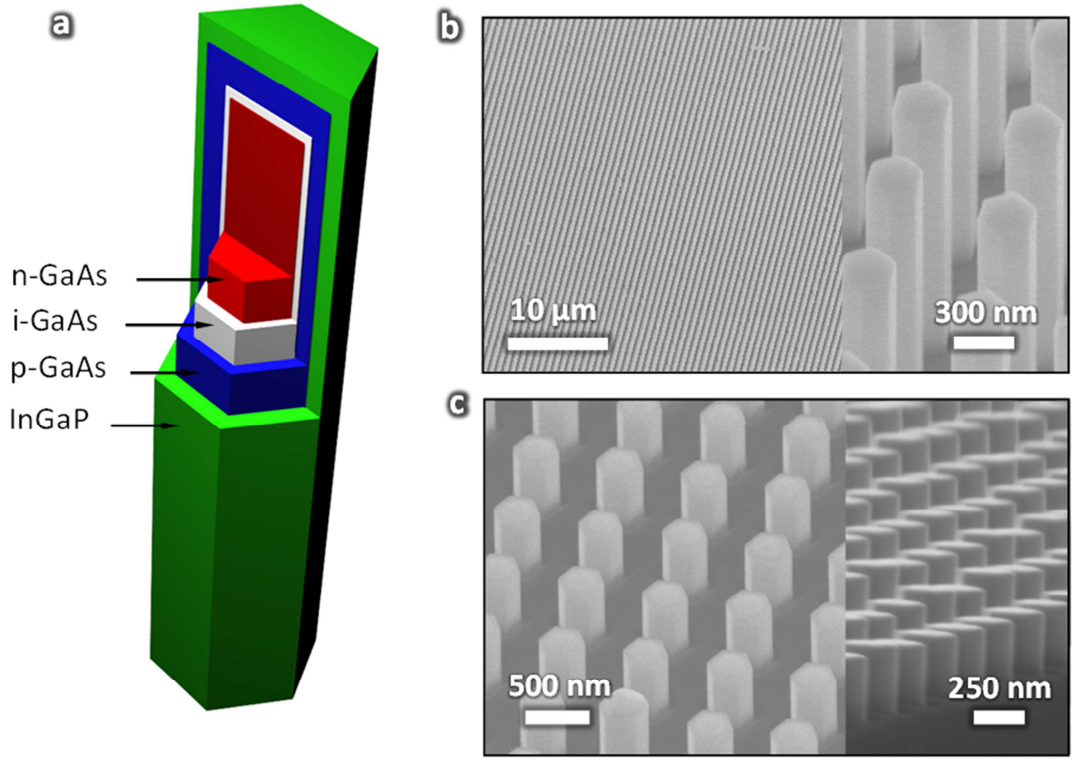

Figure 6.1. (a) 3-D illustration of the designed/fabricated NP core-multishell structure: the p-i-n radial junction is wrapped in InGaP shell to lessen surface-state-induced surface recombination. (b) Typical SEM image of vertically aligned NP arrays. (c) BCB planarization layer and etch-back step to partly expose back the NP.

The NPs are grown by means of selective-area MOCVD, without any metal catalyst to foster the synthesis that could affect the device performance. In brief, a Sn-doped GaAs n-core ($N_D \sim 1 \times 10^{17}$ cm^{-3}, from planar calibrations) with 180 nm diameter is first grown. Second, a ~10 nm intrinsic GaAs shell followed by a 40 nm Zn-doped GaAs p-shell ($N_A \sim 3 \times 10^{18}$ cm^{-3}) are formed. Lastly, a ~5 nm InGaP window layer is synthesized to mitigate NP surface recombination.[20]

This is carried out by a careful control of the heteroepitaxy in the NP in terms of temperature and flow rates during growth. The final core-multishell NP height and diameter are 1.3 μm and ~290 nm, respectively. Figure 6.1b shows a SEM picture of a typical array growth. The NPs are hexagonally faceted, arranged in a square tiling pattern. Ratios of D/P ~0.5[17] are shown to maximize the absorption in periodic GaAs NP arrays; therefore a pitch of 600 nm is chosen here. Subsequent to epitaxy, BCB is used to planarize the NP array and, after hard curing, etched back to expose ~350 nm tips. Figure 6.1c displays the partly exposed NPs. On the right half of the figure, a 80°-tilted SEM picture is provided: to notice the low variability in height, witnessing fairly constant growth rates for the NPs across the device.

Photocurrent spectroscopy measurements on doped-GaAs homoepitaxial layers have shown photocurrent contributions resulting from illuminating the semiconductor.[21] An estimated minority carrier diffusion length between ~0.4 μm and ~2 μm[21,22] has been extrapolated for layers at different doping concentrations. Therefore, it becomes necessary to rule out possible photocurrents generated in the substrate ($I_{PH,SUB}$) that could be recollected by the NP arrays, measuring a higher apparent short-circuit current density ($J_{SC,APP}$) given by

$$J_{SC,APP} = \frac{I_{PH,SUB}(V=0)+I_{PH,ARRAY}(V=0)}{active\ area\ array} \tag{6.1}$$

where $I_{PH,ARRAY}$ represents the actual photocurrent solely output by the NP-array solar cell. To separate the two addends, an area-dependent measurement is required. Each NP-array photovoltaic device, in fact, is grown on a cleaved 1 cm × 1 cm n-doped GaAs substrate, wherein a NP subregion is defined as active area. Equation (6.1) outlines the different current contributions. For this reason, a 0.5 mm × 0.5 mm active array area is defined.

Figure 6.2a presents a top-view SEM picture where four different transparent electrodes with

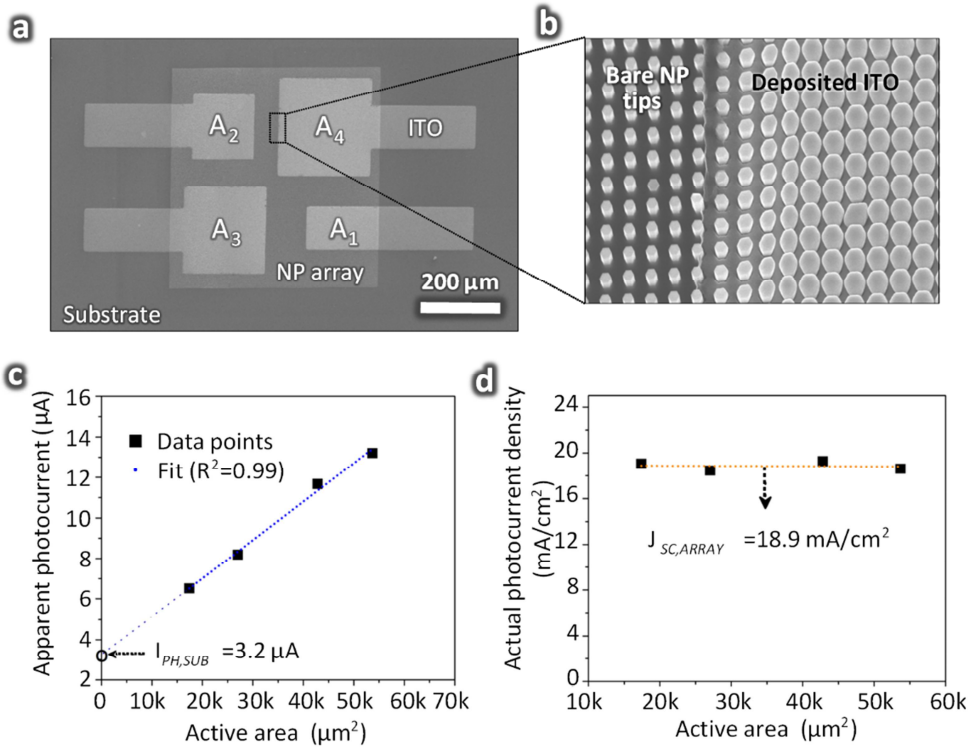

Figure 6.2. (a) Top-view SEM image of a NP array with four area-dependent transparent contacts photolithographically defined on top. (b) SEM micrograph of the zoomed-in boundary in a. To notice the difference between bare NP tips and conformal dome-shaped morphology once ITO is deposited. (c) Apparent photocurrent/active area characteristics for NP solar cells with increasing area. The extrapolated substrate photocurrent from the linear regression (R^2 = 0.99) is 3.2 µA. (d) Actual photocurrent density/active area plot showing a 18.9 mA/cm^2 current density irrespective of the device area.

increasing areas are contacting the NP-array: A_1, A_2, A_3, and A_4 correspond to NP-areas of 14410, 27030, 42830, and 53700 μm^2, respectively. The probing pads that extend outside the active regions are electrically isolated from the substrate by the BCB resin. Figure 6.2b displays a contact boundary between the bare NP tips after the planarization process and the sputtered contact that forms a dome-shaped ITO electrode. The morphology of the ITO layer is dependent on the height of etched back NP tip as presented in Fig. 6.3 which shows the morphology evolution of the dome: from absence, beginning to actual formation of the dome.

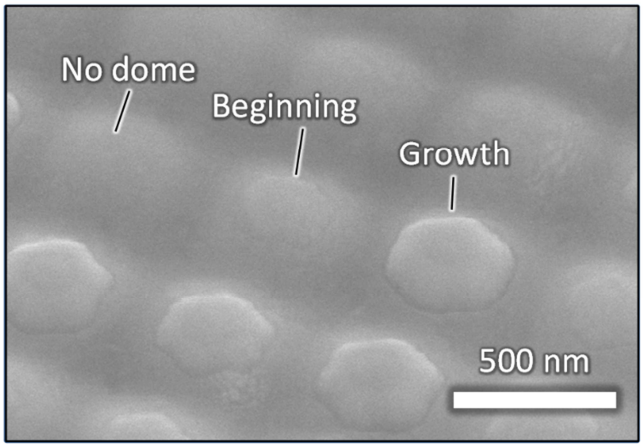

Figure 6.3. Dome formation on different NP tip heights: the process is extremely sensitive to the profile of NP tip exposed subsequent to etch-back.

A thin titanium interlayer is found to improve the ohmic behavior at the ITO/p-GaAs interface after rapid thermal annealing. Figure 6.2c plots the apparent photocurrent as a function of increasing areas. The measurements reveal a linear dependence with respect to the number of NPs contacted which are indeed responsible for the collective photovoltaic response of the devices. Nonetheless, the linear regression intercepts the y-axis at $I_{PH,SUB}$ = 3.2 μA for a zero projected active area. This result quantifies a parasitic photocurrent presumably generated by the

semiconductor substrate under AM1.5G illumination. The actual photocurrent values delivered by the NP solar cells can be extrapolated by rigidly translating downward the linear curve to intercept the origin. Subsequent to the correction for the substrate baseline, an area-independent plot of the actual photocurrent density can be formalized as presented in Fig. 6.2d.

6.3 Results and discussion

Core-multishell NP-array photovoltaic devices are tested both under dark and under AM1.5G conditions. In the dark, the ideality factor of the GaAs p-i-n NP-array is 1.86, whereas the rectification ratio at ±1 V is > 10^5. Reverse-bias leakage currents of 48 nA at -1 V indicate a high quality material, where the detrimental effect of surface states is moderated by capping the active region with a thin, lattice-matched, high bandgap InGaP shell. Under illumination, V_{OC} of 0.57 V, J_{SC} of 18.9 mA/cm^2 with *FF* up to 69% are observed as shown in the *J-V* characteristic of Fig. 6.4a.

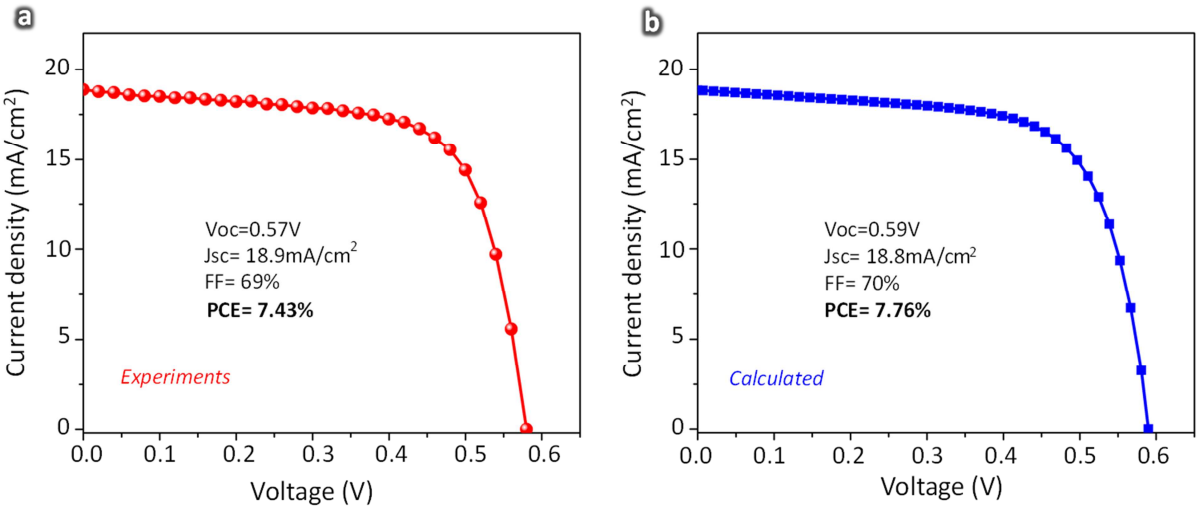

Figure 6.4. (a) Measured *J-V* characteristics of the GaAs p-i-n NP-array solar cells under AM1.5G. (b) Calculated *J-V* curve by means of FDTD simulations.

The resulting *PCE* of η = 7.43% represents a considerable improvement with respect to previous reports for GaAs NP-array photovoltaics. The measured *PCE* considers the sole photocurrent contribution generated in the NP-array. So far, GaAs-based epitaxial NW solar cells have been affected by low V_{OC} values ranging from 0.2[9] to 0.24 V,[23] without the adoption of any passivation scheme and depending on the different growth method. Part of the reason is related to the large surface-to-volume ratio involved in NP-based photovoltaics. Since the active junction increases as well as surface/interface recombination rates, InGaP window layers demonstrated to reduce the surface recombination in planar GaAs solar cells.[20] To gain insight on the electronic transport under AM1.5G, FDTD, and electrical simulations are carried out using Sentaurus TCAD software suite. The FDTD method has been widely adopted in optoelectronic modeling of NPs, enabling the analysis of subwavelength light trapping mechanisms in a wave optics framework.

Figure 6.4b displays the calculated *J-V* characteristics under light, introducing a residual surface state density $N_S = 1 \times 10^{10}$ $eV^{-1}cm^{-2}$. The major V_{OC} improvement compared to previous NP reports[9,23] can be attributed to both the epitaxial windows as well as the p-i-n junction design. In fact, p-i-n junction schemes have demonstrated higher V_{OC} compared to p-n core-shell structures[7] due to a decreased dark saturation current, for NW diameters as low as 200 nm. Nonetheless, incomplete Fermi level unpinning at the surface is responsible for a lower V_{OC} with respect to planar photovoltaics, attributed in part to a nonideal passivation. This leads to a remainder surface recombination velocity $S_{PASS} = 10^4$ cm/s after passivation. Additionally, a complete array of NWs offers a route to large area integrations, however, is much more sensitive to variations compared to single-NW photovoltaics: defective NPs across the whole array can

directly reduce the device shunt resistance. The V_{OC} of NW solar cells is an ensemble measurement of millions of miniaturized p-n junctions connected in parallel between anode and cathode, and slight variations in the electrical properties of each single NP (e.g. shunt resistance, built-in electric field, ideality factor) may severely affect the overall *J-V* characteristics.

Figure 6.5 displays the *EQE* of the corresponding photovoltaic NP devices. The experimental spectral data (blue dots), taken from 400 to 950 nm wavelength, shows maximum *EQE* values of ~70 %, with an average magnitude EQE_{AVE} > 60%. Several peaks can be noticed at different wavelengths which can be attributed to the confinement/localization of guided modes within the NP-array

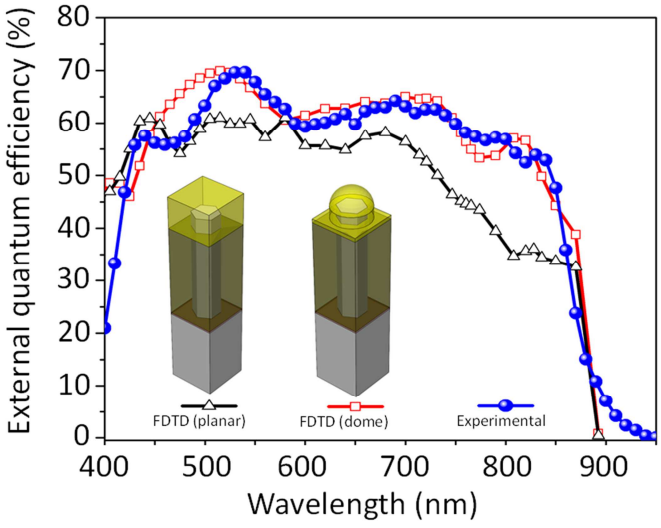

Figure 6.5. *EQE* measurements (blue dots) of the solar cells from 400 to 950 nm. FDTD simulations are carried out to analyze the impact of a planar (black triangles) and a dome-shaped ITO layer (red squares) on the final optical coupling performance. The latter shows a good fidelity compared to the measured data.

As presented in Fig. 6.2b, the overlaid ITO electrode naturally assumes a dome-shaped morphology on top the NPs due to the conformal type of deposition. The particularly rounded geometry occurs from the high nearest neighbor interaction of the sputtering plasma among NPs

in the highly packed array. The self-constituted nanostructured ITO layer has been reported to have excellent light trapping capabilities due to its unique nanophotonic effects.[24,25] Nonetheless, a high-efficiency photovoltaic device is characterized not only by enhanced solar absorption but also a remarkable collection of photocarriers which requires coupling of both optical and electrical modeling. In order to calculate the optical generation rate G_{ph}, the Poynting vector S is defined in the form of

$$G_{ph} = \frac{|\vec{\nabla}\cdot\vec{S}|}{2\hbar\omega} = \frac{\varepsilon''|\vec{E}|^2}{2\hbar} \tag{6.1}$$

where ω is the frequency of the incident light, $\hbar$ is the reduced Planck's contact, $\vec{E}$ is the electric field intensity at each grid point, and ε″ is the imaginary part of the permittivity. For the electrical modeling, optical generation profiles are first interpolated automatically to the finite-element mesh of the NWs, and then a coupled set of Poisson equation and carrier continuity equations are solved for each meshing point to compute the photocurrent at every single wavelength.

The resulting simulations (red squares and black triangles) are presented in Fig. 6.5 and directly compared to the experimental data (blue dots). The *EQE* curves are found to be in good agreement within most of the wavelength range of interest (400-900 nm). The two peaks located at λ = 520 nm and λ = 810 nm are caused by Mie resonance[26,27] that leads to a highly effective coupling of incident light into the dome-shape ITO that through a leaky channel is funneled into the NPs. Conversely, the simulated *EQE* curve with planar ITO shows no significant peaks at the aforementioned wavelengths. This is inherent to the fact that planar ITO only functions as a common antireflective coating (ARC), whereas the dome-shaped ITO creates a graded effective

refractive index profile between air and the NP, attenuating the surface reflection in a broad range of spectrum.[27] In the long wavelength range (λ > 700 nm), the *EQE* values of the structure with planar ITO drops dramatically as the incident light is less confined inside the NPs and more dissipated to the substrate with the absence of the dome-shaped ITO.

By accurately reproducing in the FDTD simulations both magnitudes and wavelengths of the measured *EQE* peaks, it is possible to consolidate a clear optical spectral analysis of the integrated NP photovoltaic devices. Figure 6.6a displays vertical cross sections of optical generation profiles through the center of the NP. Six different wavelengths are outlined: 405, 505, 600, 700, 808, and 892 nm. At λ = 405 nm where the absorption length of GaAs is fairly short, the majority of the photocarriers are generated at the surface of the NP, being the most sensitive to surface recombination and thus resulting in a relatively lower measured *EQE*.

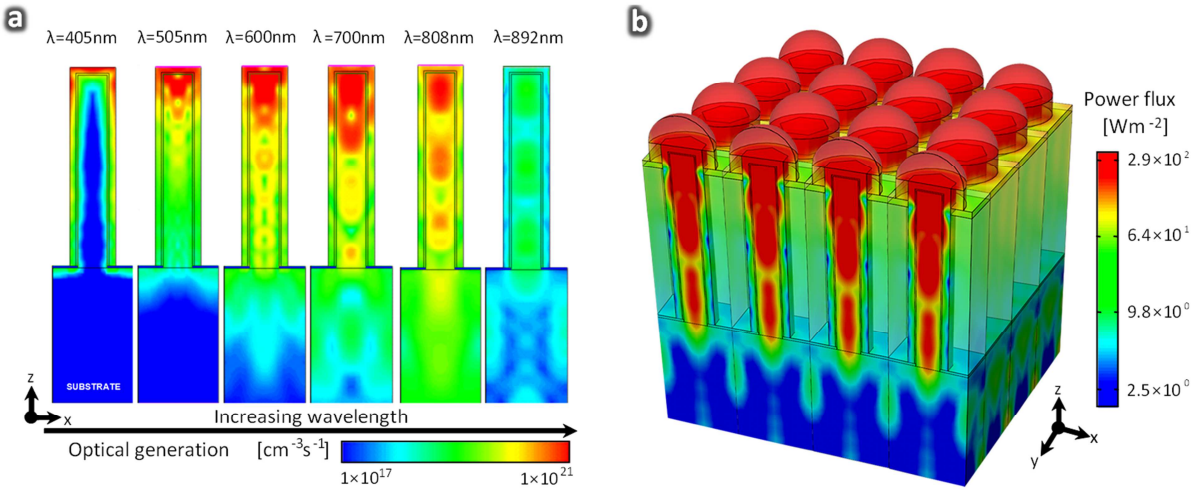

Figure 6.6. (a) Optical generation profiles calculated by FDTD for wavelengths at 405, 505, 600, 700, 808, and 892 nm. Color map is common to all six profiles. Through the dome-shaped ITO, the light is coupled into the NP-array, penetrating deeper into the semiconductor material at longer wavelengths. (b) Integrated-AM1.5G optical power flux within the periodic structure. Each ITO dome acts as a subwavelength nanolens, concentrating the optical power in the active NP region.

At longer wavelengths, the optical field is penetrating deeper into the internal part of the NP, generating electron-hole pairs more evenly distributed along the core-multishell structure. This is witnessed by higher *EQE* values. Due to the fact that the NP size is comparable to the wavelength,[28] a higher portion of the carriers is generated where the constructive interference of light takes place.

The nanostructured ITO efficiently concentrates the light from the top portion of the NP. As a consequence, the photogeneration rate is greatly increased. In other words, the dome-shaped ITO acts as a nanolens layer on top of the NP-array, where the effective focal point is wavelength-dependent: the high optical generation region (red lobes) originating from the top of the NP migrates into the NP body for increasing wavelengths, as revealed by Fig. 6.6a. Notably, these results demonstrate the confinement of light into nanoscale volumes, with minimal photogeneration located at the substrate. Reducing the amount of the active absorber represents a unique advantage of nanostructures, enabling practical low-cost photovoltaics. This demonstrates the capability to recycle the substrate for consecutive growths, further reducing production costs. Figure 6.6b exhibits a 3D power flux density map of a 4-by-4 array of NPs under AM1.5G, with the front row cut away from the middle of the structure. The figure confirms the coupling of incident light into a 2D array of nanolenses and subsequently into the whole NP array. A large portion of the power density is concentrated within the NP, leading to an increased local density of optical states. The map is calculated considering a solar-spectrum-weighted incident power, where both subwavelength effects from an infinitely periodic NP array and a domeshaped ITO array are synergistically modeled.

In conclusion, this chapter presents 7.43% efficiencies for periodic arrays of GaAs core-multishell NP solar cells and correlates *J-V* and *EQE* measurements with FDTD simulations for a full-wave optoelectronic analysis of the devices. Area-dependent photocurrent characterization quantifies substrate current contributions that could lead to an overestimation of short-circuit current densities in NP-based solar cells. *J-V* calculations highlight a residual surface state density $N_T = 1 \times 10^{10}$ eV^{-1} cm^{-2} after epitaxial passivation. Full-wave calculations fit with good fidelity the *EQE* experimental data and allow extracting realistic photogeneration profiles and delving into the spectral behavior of the fully integrated NP photovoltaic device. High optical absorption arising from the NP matrix is a necessary but not sufficient condition to achieve high-efficiency NP-based photovoltaics: cohesive optical and electrical investigation of the complete solar cells is paramount to correlate theoretical calculations with experimental results. This study demonstrates that epitaxial window layers are necessary to reduce surface recombination and the dome-shape of the nanostructured ITO layer can greatly foster the light coupling within the periodic NP array with respect to flat ARC depositions. The confinement of optical power flux inside the nanostructures effectively reduces the amount of active absorber with respect to thin-film architectures, enabling substrate recycling for practical low-cost photovoltaics.

6.4 References

1. Greytak, A. B., Barrelet, C. J., Li, Y., Lieber, C. M. Semiconductor nanowire laser and nanowire waveguide electro-optic modulators, *Appl. Phys. Lett.* **87**, 151103 (2005).

2. Huang, M. H. Mao, S., Feick, H., Yan, H., Wu, Y., Kind, H., Weber, E., Russo, R., Yang, P. Room-temperature ultraviolet nanowire nanolasers, *Science* **292**, 1897-1899 (2001).

3. Fan, Z., Ho, J. C., Jacobson, A. Z., Razavi, H., Javey, A. Large-scale, heterogeneous integration of nanowire arrays for image sensor circuitry, *PNAS* **105**, 11066-11070 (2008).

4. Hayden, O., Agarwal, R., Lieber, C. M. Nanoscale avalanche photodiodes for highly sensitive and spatially resolved photon detection, *Nat. Mater.* **5**, 352-356 (2006).

5. Bulgarini, G., Reimer, M., Hocevar, M., Bakkers, E., Kouwenhoven, L., Zwiller, V. Avalanche amplification of a single exciton in a semiconductor nanowire, *Nat. Photonics* **6**, 455-458 (2012).

6. Goto, H., Nosaki, K., Tomioka, K., Hara, S., Hiruma, K., Motohisa, J., Fukui, T. Growth of core-shell InP nanowires for photovoltaic application by selective-area metalorganic vapor phase epitaxy, *Appl. Phys. Express* **2**, 035004 (2009).

7. Kempa, T. J., Cahoon, J. F., Kim, S.-K., Day, R. W., Bell, D. C., Park, H.-G.; Lieber, C. M. Coaxial multishell nanowires with high-quality electronic interfaces and tunable optical cavities for ultrathin photovoltaics, *PNAS* **109**, 1409-1412 (2012).

8. Tang, J., Huo, Z., Brittman, S., Gao, H., Yang, P. Solution-processed core-shell nanowires for efficient photovoltaic cells, *Nat. Nanotechnol.* **6**, 568-572 (2011).

9. Czaban, J. A., Thompson, D. A., LaPierre, R. R. GaAs core-shell nanowires for photovoltaic applications, *Nano Lett.* **9**, 148-154 (2009).

10. Cao, L., White, J.S., Park, J.S., Schuller, J.A., Clemens, B.M., Brongersma, M.L. Engineering light absorption in semiconductor nanowire devices, *Nat. Mater.* **8**, 643-647 (2009).

11. Kayes, B., Atwater, H. Comparison of the device physics principles of planar and radial p-n junction nanorod solar cells J. Appl. Phys. 97, 114302 (2005).

12. Tsakalakos, L., Balch, J., Fronheiser, J., Korevaar, B. A. Silicon nanowire solar cells, *Appl. Phys. Lett.* **91**, 233117 (2007).

13. Wei, W., Bao, X., Soci, C., Ding, Y., Wang, Z. Wang, D. Direct heteroepitaxy of vertical InAs nanowires on Si substrates for broadband photovoltaics and photodetection, *Nano Lett.* **9**, 2926-2934 (2009).

14. Chen, R., Tran, T.-T., Ng, K., Ko, W. S., Chuang, L., Sedgwick, F., Chang-Hasnain, C. Nanolasers grown on silicon, *Nat. Photonics* **5**, 170-175 (2011).

15. Weisse, J., Lee, C., Kim, D., Zheng, X. Fabrication of flexible and vertical silicon nanowire electronics, *Nano Lett.* **12**, 3339-3343 (2012).

16. Kosten, E., Warren, E., Atwater, H. Ray optical light trapping in silicon microwires: exceeding the 2n2 intensity limit, *Opt. Express* **4**, 3316-3331 (2011).

17. Wen, L., Zhao, Z., Li, X., Shen, Y., Guo, H., Wang, Y. Theoretical analysis and modeling of light trapping in high efficiency GaAs nanowire array solar cells, *Appl. Phys. Lett.* **99**, 143116 (2011).

18. Kailuweit, P., Peters, M., Leene, J., Mergenthaler, K., Dimroth, F., Bett, A. Numerical simulations of absorption properties of InP nanowires for solar cell applications, *Prog. Photovolt: Res. Appl.* **20**, 945-953 (2011).

19. Wu, P., Anttu, N., Xu, H., Samuelson, L., Pistol, M.E. Colorful InAs nanowire arrays: from strong to weak absorption with geometrical tuning, *Nano Lett.* **12**, 1990-1995 (2012).

20. Plá, J., Barrera, M., Rubinelli, F. The influence of the InGaP window layer on the optical and electrical performance of GaAs solar cells, *Semicond. Sci. Technol.* **22**, 1122-1130 (2007).

21. Muralidharan, E. Ploog, K. Determination of diffusion length of minority carriers in epitaxial layers by photocurrent spectroscopy , *Appl. Phys. A: Mater. Sci. Process.* **49**, 527-531 (1989).

22. Loferski, J., Roessler, B., Crisman, E., Chen, Y., Kaul, L., Walker, J. *NASA Ninth semiannual report* Brown University (1974).

23. Cirlin, G.E., Bouravleuv, A.D., Soshnikov, I.P., Samsonenko, Y.B., Dubrovskii, V.G., Arakcheeva, E.M., Tanklevskaya, E.M., Werner, P. Photovoltaic properties of p-doped GaAs nanowire arrays grown on n-type GaAs(111)B substrate, *Nano. Res. Lett.* **5**, 360–363 (2010).

24. Ferry, V. E., Polman, A., Atwater, H. A. Modeling light trapping in nanostructured solar cells, *ACS Nano* **11**, 10055-10064 (2011).

25. Zhu, J., Hsu, C.-M., Yu, Z., Fan, S., Cui, Y. Nanodome solar cells with efficient light management and self-cleaning, *Nano Lett.* **10**, 1979-1984 (2010).

26. Spinelli, P., Verschuuren, M. A., Polman, A. Broadband omnidirectional antireflection coating based on subwavelength surface Mie resonators, *Nat. Commun.* **3**, 692-696 (2012).

27. Leem, J. W., Yu, J. S. Indium tin oxide subwavelength nanostructures with surface antireflection and superhydrophilicity for high-efficiency Si-based thin film solar cells, *Opt. Express* **20**, A431-A440 (2012).

28. Li, J., Yu, H., Li, Y. Solar energy harnessing in hexagonally arranged Si nanowire arrays and effects of array symmetry on optical characteristics, *Nanotechnology* **23**, 194010 (2012).

Chapter 7

Summary

7.1 Conclusions

Nanopillar photovoltaics represents an emerging alternative to standard solar cell technology to achieve a low cost, high efficiency route for solar electricity. The presented thesis work delves into the device design, fabrication, and testing/characterization of NP-array solar cells to verify the potential of 3D radial photovoltaic junctions with respect to traditional 2D planar cells. Catalyst-free selective-area epitaxy is utilized as a tool to control the axial/radial nanostructure synthesis. The advantage of a radial junction geometry is represented by the orthogonalization of the vertical solar photon absorption with respect to the radial/concentric charge carrier collection.[1] The optical absorption is dependent on the NP height, whereas photogenerated carriers are separated along the built-in electric field of the core-shell junction and collected at the respective electrodes. Hence, the NP radius is considerably smaller that the minority carrier diffusion length.[2] Despite the drastic material reduction compared to thin-films, NP solar cells can be considered optically 'thick' while electrically 'thin'. The former concept refers to the fact that NP arrays sustain resonant trapping effects to enhance the photon absorption, achieving absorption values close to 100% with as low as 10% of semiconductor material utilized.[3] The latter concept addresses an efficient carrier collection that minimizes the mean path from the photogeneration of a carrier to its effective extraction. The thesis demonstrated the realization of NP-array photovoltaics exploiting either hybrid organic-inorganic junctions or all-semiconductor core-shell junctions. The

combination of spinnable conjugated polymers and GaAs semiconducting NPs results advantageous in terms of processability, ease of fabrication, and cost-effectiveness. Nonetheless, spin-casting deposition limits the control and 3D coverage due to the high aspect ratio of the nanostructures. Electrodeposition of conducting polymers by means of cyclic voltammetry allows to intimately tune both the properties of the polymer (e.g. conductivity, energy levels, shell thickness) and the photo-diode (e.g. open-circuit voltage, short-circuit current, quantum yield, power conversion efficiency). An optimized hybrid PEDOT/GaAs hybrid junction reached efficiencies of 4.11%.[4] Considerable amount of research in organic solar cells is currently aimed to analyze the origin of the polymer degradation over time and prolonged exposure to ultra-violet light.[5] In order to avoid such instability, an all-semiconductor radial architecture is also investigated. The various doped regions are grown in situ during the crystal formation. Achieving transparent ohmic contacts to III-V NP devices represents an active area of investigation.[6] Particularly, the electrode Hall polarity should match the type (i.e. n or p) of semiconductor to contact. A portion of a NP-array solar cell is characterized through scanning photocurrent microscopy to highlight the photocurrent pattern: each NP acts indeed as an individual solar cell, connected in parallel with the remainder of the array. The increased surface-to-volume can be either ameliorating or detrimental to the overall device performance. Junction engineering is not only relegated to the two sides of the junction but extends to methods to lower surface state densities. NP-based devices are found to be exceptionally sensitive to surface treatments. One demonstration showed an increased *PCE* when a wide-bandgap semiconductor was epitaxially grown to cap the active radial p-n junction. Superb surface/interface qualities are necessary to challenge current state-of-the-art photovoltaics. Another paramount aspect is an efficient photon management of the fabricated solar cell. The final device, in fact, generally

comprises of insulating dielectric layers as well as a transparent top contact. The deposition of ITO naturally forms a dome shape on top of each NP. The specific morphology functions as a lens at the nanoscale, where the light field is intensified and concentrated within the NP itself. Recurring resonance peaks in external quantum efficiency are modeled through FDTD simulations. Junction engineering in conjunction with photon management are necessary to obtain efficiencies as high as 7.43%[7] for GaAs NP-array solar cells.

7.2 Future work and outlook

III-V direct bandgap NPs offer the chance to efficiently absorb solar radiation at a fraction of semiconductor material utilized in equivalent thin-film schemes. Yet, the scientific community has still a long list of open questions to answer before entering the fierce market of solar energy. The radial junction configuration is based on the notion that photons are absorbed axially whereas charge carriers are collected radially. A core-shell p-n junction creates a 3D built-in electric field profile, buried only a few tens of nanometers away from the surface. That introduces a strong dependence of the junction properties on the quality of the surface. Surface charges, surface states, mid gap electronic transitions resulting from atomic dangling bonds, and increased surface recombination velocity can be considered equivalent models used to formalize the repercussions of an imperfect NP surface onto the electrical characteristics of the diode. Indeed, surface states modify the depletion region profile of the junction,[8] which is not solely determined by doping levels anymore. Surface passivation can be realized in situ by means of wide bandgap materials (e.g. InGaP) that offer a stable solution over time. Such type of treatment aims to reduce minority carrier recombination at the surface of the nanostructure.[9] Novel materials (e.g. dielectrics or II-VI semiconductors) need to be investigated to find effective

alternatives to current passivation techniques. Additionally, axial junction geometries can be especially promising to reduce the dark saturation current (by reducing the junction area) to obtain high V_{OC} values. Remarkable research efforts on this front recently pioneered a 13.8 %[3] certified power conversion efficiency for InP arrays of nanowires based on axial p-i-n junctions. Dopant profiling remains a non-trivial measurement. Proof-of-concept techniques proposed Kelvin probe microscopy,[10] atom probe tomography,[11] direct Hall measurement,[12] capacitance-voltage profiling,[13] and field-effect transistors,[14] as tools to directly or indirectly infer the dopant distributions, level concentrations, and gradients within the doped NP crystal. Transparent electrodes cannot achieve the same contact resistance obtained with traditional metals. Novel solutions such as graphene or new alloys of conducting oxides could open up research routes to increase FF above 80%. Another viable option to boost the efficiency is to monolithically incorporate a secondary junction at a higher bandgap (e.g. InGaP, GaAsP) to harvest power from the highly energetic ultra-violet spectral region more effectively.

7.3 References

1. Mariani, G., Wong, P.S., Katzenmeyer, A.M., Leonard, F., Shapiro, J., Huffaker, D.L. Patterned radial GaAs nanopillar solar cells, *Nano Lett.* **11**, 2490-2494 (2011).

2. Kayes, B.M., Atwater, H.A., Lewis, N.S. Comparison of the device physics principles of planar and radial p-n junction nanorod solar cells, *Journ. Appl. Phys.* **97**, 114302-1-11 (2005).

3. Wallentin, J., Anttu, N., Asoli, D., Huffman, M., Aberg, I., Magnuss, M.H., Siefer, G., Fuss-Kailuweit, P., Dimroth, F., Witzingmann, B., Xu, H.Q., Samuelson, L., Deppert, K., Borgstrom, M.T. InP nanowire array solar cells achieving 13.8 % efficiency exceeding the ray optics limit, *Science* **339**, 1057-1060 (2013).

4. Mariani, G., Wang, Y., Wong, P.S., Lech, A., Hung, C.H., Shapiro, J., Prikhodko, S., El-Kady, M., Kaner, R.B., Huffaker, D.L. Three-dimensional core-shell hybrid solar cells via controlled in situ materials engineering, *Nano Lett.* **12**, 3581-3586 (2012).

5. Neugebauer, H., Brabec, C., Hummelen, J.C., Sariciftci, N.S. Stability and photodegradation mechanisms of conjugated polymer/fullerene plastic solar cells, *Sol. En. Mat. Sol. Cells* **61**, 35-42 (2000).

6. Cunningham, T.J., Guido, L.J., Beggy, J.C., Barker, R.C. Annealed indium oxide transparent ohmic contacts to GaAs, *Journ. Appl. Phys.* **71**, 1070 (1992).

7. Mariani, G., Zhou, Z., Scofield, Z., Huffaker, D.L. Direct-bandgap epitaxial core-multishell nanopillar photovoltaics featuring subwavelength optical concentrators, *Nano Lett.* **13**, 1632-1637 (2013).

8. Björk, M.T., Schmid, H., Knoch, J., Riel, H., Riess, W. Donor deactivation in silicon nanostructures, *Nat. Nanotechnol.* **4**, 103 (2009).

9. Yablonovich, E., Skromme, B. J., Bath, R.; Harbison, J. P., Gmitter, T. J. Band bending, Fermi level pinning, and surface fixed charge on chemically prepared GaAs surfaces, *Appl. Phys. Lett.* **54**, 555-557 (1989).

10. Koren, E., Hyun, J.K., Givan, U., Hemesath, E.R., Lauhon, L.J., Rosenwaks, Y. Obtaining uniform dopant distributions in VLS-grown Si nanowires, *Nano Lett.* **11**, 183-187 (2011).

11. Moutanabbir, O., Isheim, D., Blumtritt, H., Senz, S., Pippel, E., Seidman, D.N. Colossal injection of catalyst atoms into silicon nanowires, *Nature* **496**, 78-82 (2013).

12. Storm, K., Halvardsson, F., Heurlin, M., Lindgren, D., Gustafsson, A., Wu, P.M., Monemar, B., Samuelson, L. Spatially resolved Hall effect measurement in a single semiconductor nanowire, *Nat. Nanotech.* **7**, 718-722 (2012).

13. Garnett, E.C., Tseng, Y.C., Khanal, D.R., Wu, J., Bokor, J., Yang P. Dopant profiling and surface analysis of silicon nanowires using capacitance-voltage measurements, *Nat. Nanotech.* **4**, 311-314 (2009).

14. Xie, P., Hu, Y., Fang, Y., Huang, J., Lieber C.M. Diameter-dependent dopant location in silicon and germanium nanowires, *PNAS* **106**,15254-15258 (2009).